Revision 3

Word count: 14,330

Mineral and crystal chemical study of pseudo-*C*2/*m* non-metamict chevkinite-(Ce): an investigation into the intracrystalline distribution of LREE, HREE, and octahedral cations in samples from the Azores and Pakistan

SUSANNA CARBONIN [1,*] , FILIPPO RIDOLFI [2] , ALBERTO RENZULLI [3] , ELENA BELLUSO [4] , LUCA NODARI [5] , FEDERICA LIZIERO [1,**] , AND SILVANA CAPELLA [4]

[1]Dipartimento di Geoscienze, University of Padova, Via Gradenigo 6, I-35131 Padova.
*Present address: Via Giovanni da Nono 6 Bis, I-35127 Padova.<susi.carbo@hotmail.co.uk>
**<federica.liziero@unipd.it>
[2]Institut für Mineralogie, Leibniz Universität, Callinstr. 3, D-30167 Hannover.
<f.ridolfi@mineralogie.uni-hannover.de>
[3]Dipartimento di Scienze Pure e Applicate (DiSPeA), University of Urbino, Via Ca' Le Suore 2-4, I-61029 Urbino. <alberto.renzulli@uniurb.it>
[4]Dipartimento di Scienze della Terra, University of Torino, Via Valperga Caluso 35, I-10125 Torino.
<elena.belluso@unito.it><silvana.capella@unito.it>
[5]Istituto di Chimica della Materia Condensata e di Tecnologie per l'Energia, Consiglio Nazionale delle Ricerche, (ICMATE-CNR), Corso Stati Uniti 4, I-35127 Padova. <luca.nodari@cnr.it>

ABSTRACT

The cation distribution among the A, B, C, and D sites of 13 crystals of chevkinite-(Ce) by X-ray single crystal diffraction and electron microprobe analyses is reported in this article. The general formula of chevkinite-(Ce) is $A_4BC_2D_2O_8(Si_2O_7)_2$, where A = REE, Ca, Th, Sr; B = Fe, Mn, Mg; C = Fe, Ti, Nb, Zr, Mg, Al; and D = Ti. Ten crystals come from quartz-bearing syenite samples of Agua de Pau (Azores Islands), three from euhedral chevkinite crystals of a quartz-bearing pegmatite from Tangir Valley, north-western Pakistan. The real space group for these samples is $P2_1/a$, but the average structure in space group $C2/m$ was used for structural refinement and further interpretation. Cation distribution was determined by minimization of the function $f_{\Sigma N_\sigma^2}$ that represents the sum of the squared numbers of standard deviation by which each expected quantity differs from the calculated one. Both X-ray diffraction and electron microprobe data were considered in minimization. Our results show that the two non-equivalent A sites are occupied dominantly by REE and Ca, distributed mainly as a function of their ionic size. Lanthanum enters only the 10-coordinated A2 site whereas heavier and smaller REE enter only the 8-coordinated A1. Furthermore, comparison between bond valence sum and formal charge revealed highly stretched bonds for the A1 polyhedron, suggesting that bond lengths are too long for HREE. These findings can help better characterize the well-known ability of chevkinite to fractionate LREE from HREE. The Azores chevkinite is particularly enriched in Nb relative to its host rock. Our results show that Ti occupancy in the D sites can be as low as ca. 50% due to the presence of significant amounts of Nb, besides Fe and Zr. For two Azores crystals showing patchy zoning, a complex history of late-stage crystallization is inferred, with multiple events of Ca and REE enrichments. One of these crystals showed the best structure refinement, implying that late-magmatic to deuteric alteration stages did not affect its crystallinity. The CaO content of Azores chevkinites practically spans the entire chevkinite field in the chevkinite/perrierite CaO vs. FeO discrimination diagram. In addition, we identified possible structural stability limits that can be linked to the occupancy of the B site at high CaO, and of the C sites at high FeO contents. The Pakistan chevkinites were also analyzed by Mössbauer spectroscopy. Only one Fe^{3+} component was identified, which occupies the C sites. Among the two ferrous doublets, the component with the highest isomeric shift value is Fe^{2+} entering the most distorted crystallographic site B, while the other, representative of a less distorted octahedral site, corresponds to Fe^{2+} entering the D sites.

Key words: chevkinite, crystal structure, non-metamict, deuteric alteration, Mössbauer spectroscopy.

INTRODUCTION

Chevkinite-(Ce), a REE (Rare Earth Elements)-Ti-Fe-rich sorosilicate, is a member of the chevkinite group of minerals (CGM, Macdonald et al. 2002) with the general formula $A_4BC_2D_2O_8(Si_2O_7)_2$, where A = REE, Ca, Th, Sr; B = Fe, Mn, Mg; C = Fe, Ti, Nb, Zr, Mg, Al; and D = Ti. While the A sites, hosting relatively large cations (i.e., REE, Ca, Sr), are at least seven-coordinated by oxygen atoms, the remaining B, C, and D sites all have distorted octahedral coordination, hosting smaller cations. Chevkinite-(Ce) belongs to the chevkinite subgroup, with the other subgroup represented by perrierite with the same general formula but a different structure (Sokolova et al. 2004; Sokolova and Hawthorne 2004; Macdonald et al. 2019).

Macdonald et al. (2019) extensively reviewed the CGM and highlighted their compositional diversity and occurrence in a wide range of crustal, and some extraterrestrial, environments. CGM, when found, *inter alia*, i.e., as single crystals or as inclusions in early formed minerals of plutonic or subvolcanic rocks, can influence trace element distribution during fractional crystallization (Macdonald et al. 2019).

The modular character of the chevkinite group of minerals, based on a rutile layer and a silicate layer stacked along *c**, was recently described by Malcherek et al. (2021). The rutile layer, topologically identical to a (110) layer of the rutile structure, is composed of alternatively attached edge-sharing C chains and edge-sharing D chains running parallel to the *b*-axis. The other basic module, the silicate layer, is composed of the A1 and A2 polyhedra, the Si_2O_7 disilicate group, and the B octahedron (Fig. 1). When comparing structural data from the literature, inconsistencies can be found because of the considerable non-uniformity in the naming of the sites (e.g., Popov et al. 2001; Yang et al. 2002) and because of the different choices of the origin of the unit-cell (e.g., Calvo and Faggiani, 1974; Sokolova et al. 2004). According to the nomenclature adopted here (Calvo and Faggiani 1974; Yang et al. 2002), the C chain octahedra are represented by the C1 sites, and the D chain octahedra are represented by the two crystallographically independent C2A and C2B sites.

Different space groups are recognized in the chevkinite subgroup: $C2/m$ in chevkinite-(Ce), polyakovite-(Ce) $(REE,Ca)_4(Mg,Fe^{2+})(Cr,Fe^{3+})_2(Ti,Nb)_2Si_4O_{22}$, and delhuyarite-(Ce) $Ce_4Mg(Fe^{3+}W)\square(Si_2O_7)_2O_6(OH)_2$; $P2_1/a$ in strontiochevkinite $(Sr_2[La,Ce]_{1.5}Ca_{0.5})_4Fe^{2+}{}_{0.5}Fe^{3+}{}_{0.5}(Ti,Zr)_2Ti_2Si_4O_{22}$, and dingdaohengite-(Ce) $Ce_4Fe^{2+}Ti_2Ti_2(Si_2O_7)_2O_8$; $P2_1/m$ in christofschäferite-(Ce) $(Ce,La,Ca)_4Mn^{2+}(Ti,Fe^{3+})_3(Fe^{3+},Fe^{2+},Ti)(Si_2O_7)_2O_8$. However, structural varieties are not always due to compositional diversity. Li et al. (2005) successfully refined the crystal structure of a Ti- and Fe-rich chevkinite-(Ce), later defined as dingdaohengite-(Ce) (Xu et al. 2008), in both $C2/m$ and $P2_1/a$ space groups and established $P2_1/a$ as the true space group in which $h + k = 2n$ reflections were systematically strong and reflections with $h + k = 2n + 1$ systematically weak (pseudo-$C2/m$). According to Stachowicz et al. (2019a, 2019b), one Nb-rich chevkinite-(Ce) from the Biraya metal deposit (Russia) formed in space group $C2/m$ at relatively high temperature although, after a sufficiently long time, it might reorganize to $P2_1/a$ lower symmetry.

Chevkinite chemical composition and the corresponding formulae have been extensively investigated over the past four decades (e.g., Segalstad and Larsen 1978; McDowell 1979; Harding et al. 1982; Haggerty and Mariano 1983; Platt et al. 1987; Čech et al. 1988; Imaoka and Nakashima 1994; Kopylova et al. 1997; Macdonald and Belkin 2002; Macdonald et al. 2002; Troll et al. 2003; Vlach and Gualda 2007; Macdonald et al. 2009, 2012, 2013; Shellnutt and IIzuka 2013; Muhling et al. 2014). Despite the early studies of Bonatti (1959), Pen and Pan (1964), Bonatti and Gottardi (1966) and Calvo and Faggiani (1974) on chevkinite crystal structure, only a few recent investigations use both chemical and site occupancy refinement data to obtain cation distribution among the different sites (Popov et al. 2001; Yang et al. 2002; Sokolova et al. 2004; Li et al. 2005; Holtstam et al. 2017; Stachowicz et al. 2019a, 2019b; Nagashima et al. 2020) with the scattering curve(s) employed to refine site occupancies assumed to approximate the true number of electrons per site (Dollase 1971; Hawthorne et al. 1995). However, some exceptions are known: for example, for the octahedral B, C, and D sites, cation partitioning in strontiochevkinite is based only on chemical analysis, lacking structural refinement data (Haggerty and Mariano 1983); in christofschäferite-(Ce), occupancies are considered according to the interatomic distances and bond valence calculations (Chukanov et al. 2012). Even fewer studies report the site occupancy refinement values at the two non-equivalent A1 and A2 sites (Yang et al. 2002; Li et al. 2005; Holtstam et al. 2017; Stachowicz et al. 2019b; Nagashima et al. 2020), which might result in non-uniform distribution of REE, Ca and other minor elements (e.g., Sr, Th) between the two sites.

Due to the presence of Th as a minor component of chevkinite, in relatively old rocks, CGM are usually metamict, and samples' partial metamictization can have a dramatic effect on site occupancy calculations (Sokolova et al. 2004) making the task of assigning site population even more difficult. It has long been known that the calculation of a structural formula for metamict chevkinite is particularly difficult due to the complex and extensive substitutions of ions (Jaffe et al. 1956). More recently, Carbonin et al. (2005) identified problems of non-stoichiometry in metamict chevkinite from a Permo-Triassic syenite in the Alto Paraguay Province. Stachowicz et al. (2019a, 2019b) confirmed how zoning and metamictization in Nb-rich chevkinite-(Ce) from Biraya (Russia) led to considerable difficulties in reconciling compositions derived by electron microprobe analysis with those obtained by refinement of site occupancies from X-ray diffraction. In addition, complex zoning in CGM may be due to secondary processes such as late-stage hydrothermal (i.e., deuteric) and/or to metasomatic alteration, leading to the introduction and/or removal of chemical components in the magmatic-hydrothermal system through the interaction of the host rock with fluids (Macdonald et al. 2019; and references therein).

As metamict samples are partly to completely amorphous, heat treatment (i.e., annealing) is needed to improve or recover their crystallinity (Lima de Faria 1962; Mitchell 1966; Čech et al. 1988; Popov et al. 2001; Sokolova et al. 2004; Muhling et al. 2014; Holtstam et al. 2017; Stachowicz et al. 2019b). However, despite improving X-ray pattern, heat treatment generally produces a slight shrinkage of unit cell dimensions (Mitchell 1966). Furthermore, annealing experiments are conducted under different conditions of heating and cooling times, temperature, and fO_2, changing the oxidation state of CGM (Popov et al. 2001; Sokolova et al. 2004) or causing a redistribution of cations between crystallographic sites (Stachowicz et al. 2019b). To overcome these difficulties, Muhling et al (2014) suggested performing crystal chemical studies on non-metamict chevkinite only. Therefore, for high-quality structure refinement of CGM, geologically young and defect-free samples are needed. Non-metamict chevkinites were also useful for dating relatively young high-silica rhyolites by the ion microprobe ^{238}U-^{230}Th method (Vasquez et al. 2014).

This study is based on the crystallographic and crystal chemistry results obtained by Liziero (2008, unpublished PhD thesis) on:

1. non-metamict chevkinite crystals from the Azores Islands (hereafter AZ chevkinite), found within the silica-oversaturated syenite ejecta (LdF1, LdF4, LdF5) of the pumice fall deposit, which erupted during the 5 ka-old Plinian eruption of Fogo-A (caldera of Agua de Pau, Lagoa do Fogo, São Miguel Island, Azores Islands) (e.g., Walker and Croasdale 1970; Moore 1991; Widom et al. 1992, 1993; Ridolfi et al. 2003);
2. a non-metamict euhedral chevkinite crystal (hereafter PAK chevkinite) of exceptional size (3x3x1 cm) from a pegmatite of the Chilas Complex (Upper Cretaceous, ca. 85 Ma) in north-western Pakistan, Tangir Valley.

Preliminary investigation was done using transmission electron microscopy (TEM), and high-resolution transmission electron microscopy (HRTEM). Backscattered electron (BSE) images were acquired from representative thin sections of the chevkinite host rocks. Single-crystal X-ray diffraction and electron microprobe analyses were then carried out on selected chevkinite crystals with the aim of determining a cation distribution, complemented by Mössbauer spectroscopy when possible. To allocate all the chemical species into the A, B, C, and D sites, a computer program was written *ad hoc*. To the best of our knowledge, this study represents the first attempt to determine partitioning of each analyzed rare earth element and of Ca, Sr, and Th into the two non-equivalent A1 and A2 sites of the CGM, using both chemical and site occupancy refinement data.

SAMPLES, ANALYTICAL, AND COMPUTATION METHODS

Geological and petrological frameworks of the chevkinite-bearing rocks

Chevkinite from the silica-saturated/oversaturated syenite ejecta found within the pumice fall deposit of the 5-ka old Plinian eruption of Fogo A (caldera of Agua de Pau; Lagoa do Fogo, São Miguel Island, Azores Islands) was first analyzed by Ridolfi et al. (2003). Modal mineralogy of the syenites consists of 82-95% feldspar, 0-8% amphibole, 0-3% clinopyroxene, 0-3% annite, 1-5% Fe-Ti oxide, and 0-5% quartz. Chevkinite crystallized as subhedral to anhedral crystals interstitially between the feldspar crystal mush, from a late-stage residual liquid highly enriched in volatiles, alkalis, High Field Strength Elements (HFSE) and REE. Besides chevkinite, accessory minerals are represented by apatite, britholite-(Ce), titanite, aenigmatite, zircon, pyrochlore, dalyite, and thorite (Ridolfi et al. 2003; Ridolfi 2004). These weakly peralkaline syenites formed at low depth (subvolcanic environment) and are slowly cooled equivalents of the erupted trachytic magma.

The chevkinite samples from Pakistan come from a pegmatite consisting of hornblende-, pyroxene-, plagioclase-, K-feldspar-, quartz-, and locally epidote-bearing pegmatites (with up to meter-size hornblende crystals) belonging to a leucocratic lithotype of the Chilas Complex. The Chilas complex (ca. 85 Ma; Zeitler 1985; Schaltegger et al. 2002) consists of (i) a modally layered to homogeneous gabbronorite with subordinate (quartz) diorite and tonalite and (ii) an ultramafic sequence (Khan et al. 1989; Jagoutz et al. 2007) intruded into the Kohistan batholith during an intra-arc rifting phase at the base of the fossil Jurassic-Cretaceous Kohistan island arc. The latter was later sandwiched between the Indian and Asian plates during the Himalayan collision (Searle et al. 1999). Pegmatites and hornblendites of the Chilas Complex may occur within both the plagioclase-dominated mafic gabbro-norite sequence (also including gabbro, quartz-diorite, and tonalites) or at the contact zone with the ultramafites.

Methods

Quantitative chemical electron microprobe analyses (EMPA) were performed at the Istituto di Geoscienze e Georisorse (IGG) CNR Padova using a Cameca/Camebax Microbeam electron microprobe in the first part of the work and a Cameca Sx50 in the final stage of the study. Operating conditions were set at 20 kV accelerating voltage and 20 nA beam current, with peak count times in the range 20 to 50 s and background count times half of those on the element peak. Since accurate analysis of REE minerals involves considerable difficulty due to interferences in the complicated *L* wavelength series of the X-ray spectra, we used the following setting to obtain good-quality data (Exley 1980; Macdonald and Belkin 2002; Ridolfi et al. 2006): La, Ce, and Y were analyzed on the $L\alpha_1$ peaks, while Pr, Nd, Sm, and Gd were analyzed on the $L\beta_1$ peaks, both with a LiF analyzing crystal (Exley 1980). The following standards were used: REE phosphates for REE; synthetic oxides for Mg, Al, Ti, Mn, Fe, Th; wollastonite for Ca and Si; pure metallic elements for Zr and Nb. Acquisition data were constantly monitored against representative standards. Analyses were carried out after checking I_{xstd}/ I_{std} to be 1.00 ± 0.01 for each element, where I_{xstd} was the intensity of the analyzed standard and I_{std} the intensity of the same standard measured after each element calibration. Although reported in the literature (e.g., Macdonald and Belkin 2002), the fluorine content of CGM was not measured. Due to complete overlap of F*K*α peak with Ce*M*-lines, F values previously determined by EMPA measurements were considered to be in error and therefore discarded (A. Fioretti, personal communication; see also Belkin et al. 2009). Detection limits were ca. 1000 ppm for REE; between 600 and 800 ppm for Zr, Nb, Sr, Y, Th; ca. 300 ppm for Fe and Mn; and under 200 ppm for Si, Ti, Ca, Mg, Al. X-ray counts were converted into oxide weight percentages using the PAP correction program provided by Cameca.

Backscattered electron (BSE) imaging and chemical mapping were determined on representative thin sections of AZ samples using the JEOL JSM-7610F field emission gun scanning electron microscope (FEG-SEM) of the University of Hannover using a voltage of 20 kV.

Particle morphology, structural characteristics, and chemical composition were investigated by transmission electron microscopy (TEM) on a Philips CM12 instrument, operating at 120 kV with a LaB6 filament and a double tilt holder, coupled with an EDS microanalysis probe (Genesis 2000 System with TEM Quant Software PV8206/31 processing system). TEM-EDS investigations were carried out at the Department of Earth Sciences, University of Torino, on about 20 micro-fragments of both AZ and PAK chevkinites. The chevkinite grains were crushed into micro-fragments in isopropyl alcohol in an agate mortar and sonicated for 10 minutes; two drops of the resulting suspension were deposited on a copper mesh grid coated with a 200 Å carbon film. The micro-fragments were observed according to all possible angles of rotation, allowed by double tilting, to check the crystallinity degree, symmetry, and possible presence of structural defects along different crystallographic directions; align crystals along the directions useful to obtain structural image; and to relate morphology with crystallographic directions. The identification of crystallographic planes and direction was achieved by comparison with simulated electron diffraction patterns obtained using CaRine Crystallography 3.1 software (Boudias and Monceau 1998). Medium-magnification images were used to examine morphology, high-resolution TEM images (HRTEM) were acquired to evaluate structural characteristics, identify local defects, and verify the absence or presence of metamict regions within grains. Symmetry evaluation and detection of sub-micrometric-scale structural defects were performed by examining the selected area electron diffraction patterns (SAED). SAED were also used both to determine crystallographic directions, correlating them with morphological features, and to obtain oriented HRTEM images.

X-ray diffraction data (XRD) for structural refinement were collected at the Department of Geosciences, University of Padova, on a Stadi4 CCD single-crystal diffractometer equipped with an area detector and with monochromatized Mo$K\alpha$ radiation. Diffraction data were collected up to $2\Theta =$ 86° using ω scan mode with a scan speed varying from 0.025 to 0.067 °/s depending on the crystal size. The total number of reflections was up to ca. 11,000. The operating conditions were 50 kV-40 mA, except for crystals 45 and 11 (50 kV-30 mA) and for crystals 74 and 75 (45 kV-30 mA). Unit-cell parameters were calculated in the 2Θ range 6°-50° (RECIPE, STOE 1999) using between ca. 2,000 and 3,000 reflections depending on crystal quality. Diffractometer alignment was calibrated by measuring the cell parameters of a stoichiometric pure spinel and a quartz crystal. On two single crystals (9 and ID) with different chemical compositions (see Table 1), unit-cell parameters were measured using a STOE STADI IV four-circle diffractometer equipped with an unfiltered Mo sealed-tube X-ray source without monochromator (Angel et al. 1997) operating at 50 kV and 40 mA and controlled by SINGLE software (Angel et al. 2000). The diffractometer was optimized for measuring the unit-cell parameters as reported in Angel et al. (2000). During the centering procedure of the selected reflections (n. refl. = 20), the effects of crystal offsets and diffractometer aberrations were eliminated from the refined peak positions using the eight-position centering method of King and Finger (1979). Unit-cell parameters were obtained by vector least-squares (Ralph and Finger 1982) using 2Θ values only. During measurement, the reflections in crystal 9 were slightly more broadened than in crystal ID. The cell edge values obtained with the area detector agreed with those obtained with the point detector within 2 and between 1 and 4 estimated standard deviations in crystals ID and 9, respectively.

One homogeneous sample of PAK chevkinite was chosen to determine the oxidation state and coordination number of Fe and compare them with the results of the EMPA analysis. 11K Mössbauer spectroscopy (MS) was performed on a conventional constant-acceleration spectrometer, with a room-temperature Rh matrix ^{57}Co source, nominal strength 1850 MBq, equipped with an ARS® closed circuit cryostat at the Department of Chemical Science, University of Padova. The sample, ca. 50 mg, was gently crushed, dispersed in petrol jelly, and placed on a sample-holder of 2 cm diameter. Effects due to thickness were checked (Rancourt et al. 1993) and found to be negligible. The spectra were fitted to Lorentzian line shape with the statistical best fit evaluated by the reduced χ^2 method. The hyperfine parameters were obtained using the standard least-square minimization technique: isomer shift (δ), quadrupole splitting (Δ), and full linewidth at half maximum (Γ) are expressed in mm s^{-1}, while the relative area (A) in %. Uncertainties were calculated using the covariance matrix and, taking into consideration the vibrations induced by the cryostat, the errors on the Fe(II) and Fe(III) absorption areas were estimated to be equal to ±8%. The experiment was performed only at 11K to obtain a more reliable estimation of the ferrous and ferric populations and better resolve the contributions of the various species.

Cation distribution was calculated to find the best fit for the experimental results. To allocate all of the chemical species into the several available sites, a program was written to search the minimum of the function $f_{\Sigma N_\sigma^2}(X_i) = \sum_{j=1}^{N} \left(\frac{E_j - C_j(X_i)}{\sigma_j} \right)^2$, where E_j is a quantity expected, $C_j(X_i)$ the same quantity calculated using parameters X_i, and σ_j the standard deviation of the quantity E_j. The minimum was searched using the symplex method (Nelder and Mead 1965). The specific symbol $f_{\Sigma N_\sigma^2}$ was chosen because this function represents the sum of the squared numbers of standard deviation by which each expected quantity differs from the calculated one. The expected quantities were those observed from chemical analysis (20) and structure refinement (10), and those derived from stoichiometry and crystal chemistry criteria (18). When measured by Mössbauer spectroscopy (i.e., in PAK chevkinite), the Fe^{3+}/Fe_{tot} was also considered. Quantities derived from chemical analysis were the 19 atoms per formula unit (apfu) plus the total number of electrons, excluding Si. The error for the Fe^{3+} atomic fraction was estimated from propagation of errors of all of the other cations and was considerably higher than its standard deviation (Table S1 and Appendix A). Quantities derived from structure refinement were the number of electrons at the A1, A2, and octahedral sites, and the octahedral mean bond distances. Quantities based on stoichiometry and crystal chemistry were the sum of the cations at each A1, A2, B, C1, C2A, C2B, Si1, Si2 site, the total number of cations per formula unit, the total number of charges for the balance, and the formal charge of each oxygen atom; regarding these constants, their uncertainties cannot be the experimental standard deviations. However, should these quantities be determined experimentally, their measure would be affected by an uncertainty. For example, the uncertainty on the total cation charge (44) can be estimated through the propagation of errors of the atomic fractions from chemical analysis; it resulted ca. 0.05 charges for homogeneous and up to ca. 0.16 for non-homogeneous samples. A value of 0.05 was applied in the minimization, obtaining very good agreement between the calculated and the expected values (Table S2). Using an error significantly lower than 0.05, i.e., 0.01, generally produced differences of a few units to the third decimal place in the obtained cation occupancies. Only in two cases (samples ID and 1), the calculated cation charge deviated from the ideal value of 44 by ± 0.04 (~ 1‰). Applying here an error of 0.01 produced differences of one unit to the second decimal place for the Fe^{3+} and the Fe^{2+} occupancies at the C1 site. The X_i parameters are the cation fractions: La, Ce, Pr, Nd, Sm, Gd, Ca, Th, and Sr both at the A1 and at the A2 sites (18); Fe^{2+}, Mg, Mn^{2+}, Ca, Zr, Y, and Fe^{3+} at the B site (7); Ti, Fe^{2+}, Fe^{3+}, Mg, Nb, Zr, and Al at each C1, C2A, and C2B sites (21); Si at each T1 and T2 sites (2). To calculate the mean bond length in the B, C1, C2A, and C2B octahedral sites, a linear contribution from each cation was assumed. Cation and anion radii were taken from Shannon (1976); the oxygen ionic radius was considered to be 1.37 Å with a mean coordination number of 3.6 (Sokolova et al. 2004). To calculate the charge at each oxygen atom, the bond valence sum (BVS, Brown 1981) was used. The bond distances for the A1 and A2 sites, where the rare earths reside, were not considered for the minimization. The lanthanides' ionic radii for the coordination numbers eight and ten are determined with less reliability than for the cations occupying the octahedral sites (Shannon 1976). Moreover, the coordination polyhedra are not regular polyhedra but rather distorted (Miyawaki and Nakai 1996).

RESULTS

Texture and chemical mapping (FEG-SEM)

SEM textural and chemical mapping was performed only on the AZ chevkinite because of the small size of euhedral to subhedral crystals (usually 70-120 and up to 250 μm), found both interstitially and as inclusions within the feldspar rims (Ridolfi et al. 2003; Ridolfi 2004). In backscattered electron (BSE) images, the crystals appear rather homogeneous (Fig. 2 A) or slightly heterogeneous (Fig. 2 B, C, D); in other cases, variations in brightness of chevkinite-(Ce) are remarkable (Fig. 2 E, F). Where chevkinite is closely associated with REE-bearing minerals, such as britholite and monazite, complex patchy zoning in Ca and REE contents is the most evident feature, with the enrichment in REE probably deriving from REE remobilization in britholite induced by deuteric alteration (Figs. 2 E, F, and 3 A, B, C, and D). In contrast, where chevkinite is not closely associated to or in contact with other REE-bearing minerals, the observed REE, Fe, and Ca-Nb zonings should be due to chemical exchange, always due to deuteric and/or metasomatic fluids, with minerals such as apatite and Fe-Ti oxides (Figs 2 D, and 3 E, F). Apatite (belonging to the britholite-apatite solid-solution), which most likely is an igneous precursor of britholite, appears extensively altered and zoned with REE. Fe-enrichment can be mostly due to late-stage magmatic crystallization from interstitial residual liquids of the syenites or associated to iron re-mobilization from magnetite and ilmenite. Ca- and Nb-rich fluxes appear to depart from the same altered apatite crystals toward chevkinite (Fig. 3 E, F) along paths which are distinct from those of the REE- and Fe-rich areas. Similarly, in the chevkinites shown in Fig. 2 C, REE-rich embayments depleted in Ca and Nb are recognizable. Thus, the above observations suggest that zoning is more evident when chevkinite is associated with other REE-bearing minerals. In contrast, when chevkinite is not surrounded by REE-bearing minerals (Fig. 2 C, D), the fluids involved in the variability of its composition appear to be associated with minerals that contain no or small amounts of REE.

A complex history of late stage magmatic to deuteric crystallization is also inferred for two crystals of chevkinite showing patchy zoning (Fig. S1). In this case, although alteration cannot be easily associated to fluids from well identified surrounding minerals, multiple events of Ca and REE enrichments have also occurred. Surprisingly, one of these patchy zoned crystals shows the best structure refinement (see XRD section), implying that its partial chemical alteration did not affect chevkinite crystallinity. Ca- and REE-rich compositions display very good analytical totals of wt% elements and good-quality mineral formulae (Fig. S1 and Table S1). Moreover, the chemical composition averaged between REE- and Ca-rich areas is found in good agreement with that derived by refinement of site occupancies using single-crystal X-ray diffraction (see XRD section).

Mineral chemistry (EMPA)

Averaged chemical spot analyses of the investigated chevkinites are reported in Table 1. On each crystal, between 10-15 spot analyses were performed. Most of the total oxides (with total Fe expressed as FeO) vary between 99.71 and 100.19 wt%. Lower total oxides (98.87 – 99.14%) in PAK chevkinite are due to significant Fe^{3+} content, as shown also by Mössbauer spectroscopy (Fe^{3+}/Fe_{tot} ratio ca. 0.55; see Mössbauer section). A recalculation of Fe_2O_3 based on stoichiometry (Droop 1987) brings the above totals to 99.40 – 99.65 wt% (Table 1). In AZ chevkinites, the heterogeneity shown in the SEM-BSE images was compared with the standard deviation values of the samples' average oxide composition (Table 1). In crystals 74 and 9, the highest standard deviations for CaO and Ce_2O_3 are caused by remarkable Ca-REE compositional variation (Table S1); moreover, the CaO contents are lowest (2.17 and 1.84 wt%, respectively) among all analyzed crystals. In contrast, crystals 1 and 75, with intermediate CaO contents (2.84 and 2.76 wt%, respectively), and ID, 11, and 44 with the highest

CaO amounts (3.67 – 3.88 wt%) are rather homogeneous. Low CaO content, as in crystals 74 and 9, appears correlated with patchy zoning observed on SEM-BSE images (Fig. 2 E, F). Conversely, Ca-enriched crystals (1, 75, 4A, ID, 11, 44) are similar to the more homogeneous chevkinites as shown in SEM-BSE images (Fig. 2 A, B), with only minimal zoning. Crystal 4GR, with relatively high standard deviations for Ca, Nb, and Fe oxides, displays chemical zoning as observed in the chevkinite of Figure 2 D.

In the chevkinite/perrierite discrimination diagram (Macdonald and Belkin 2002), the CaO and the FeO* wt% oxides of all the samples (Table S1) are located in the chevkinite field (CaO ca. 1 – 4; FeO* ca. 10 – 12 wt%), with the CaO content of the AZ chevkinites displaying the widest range (Fig. 4). PAK chevkinites show similar CaO and FeO* contents (averaging ca. 2.0 and ca. 11.5 wt%, respectively) to chevkinites from the AZ LdF1 sample (crystals 1, 75, 74, 9), while they differ in TiO_2 (16.5 – 17.2 vs. 14.4 – 15.7 wt%), ZrO_2 (0.1 – 0.2 vs. 0.3 – 0.7 wt%), Nb_2O_5 (0.4 – 0.5 vs. 3.4 – 3.9 wt%), and Fe_2O_3 (5.1 – 6.4 vs. 2.6 – 3.2 wt%) contents (Table 1). Replacing FeO* with (FeO* + MnO) in the CaO - FeO* plot does not affect the fields of the chevkinite and perrierite subgroups implying that Fe^{2+} and Mn^{2+} play a similar role in the chevkinite structure. Using the triangular plot ($CaO+SrO+MgO+Al_2O_3$) – Σ (La_2O_3 – Sm_2O_3) – FeO* (Macdonald and Belkin 2002; Macdonald et al. 2019), all of the studied chevkinites are in the field of the silica-oversaturated evolved rocks, as expected for the Azores silica-saturated to oversaturated syenite samples (Ridolfi et al. 2003) and the occurrence of quartz in both Azores syenite and Pakistan pegmatite.

Mineral formulae on the basis of 22 oxygens yield 13.1 and 13.3 total cations in AZ and PAK chevkinite, respectively (Table 2). The Fe^{3+}/Fe_{tot} ratio applied to bring cations to a total of 13 using stoichiometric criteria (Droop 1987) is on average 0.24 in AZ, while in PAK chevkinite, it is significantly higher (0.48) and close to that obtained by Mössbauer spectroscopy (0.55; see Mössbauer section). Assuming the A site filled by REE+Ca+Sr+Th and the (B+C) sites filled by the remaining cations, an excess of cations at the A site, between ca. 4.01 – 4.06 apfu, and a slight deficiency at the octahedral sites (between ca. 4.90 – 5.00 apfu) are found, which is in agreement with previous studies (Cellai et al. 1993; Parodi et al. 1994; Macdonald and Belkin 2002; Troll et al. 2003). Deviations from integer numbers are within the respective standard deviations of the atoms (Table 2). Si ranges from 3.99 to 4.06 apfu, with a tendency to be > 4.0 in most analyses, and it can therefore be considered to fill the tetrahedral site alone. The Ca range is rather wide in AZ (0.42 – 0.84 apfu), more limited in PAK (0.43 – 0.51 apfu) chevkinites. In all of the studied chevkinites, the dominant REE are the light REE (LREE): Ce 1.65 – 1.87, La 0.78 – 1.10, Nd 0.38 – 0.62, and Pr 0.12 – 0.18 apfu, whereas Sm and Gd are very low (0.03 – 0.05 and 0.01 – 0.02 apfu, respectively). On average, La/Ce and La/Nd ratios are 0.6 and 2 in AZ and 0.4 and 1.3 in PAK crystals, respectively. Chondrite-normalized ratio $(La/Nd)_{CN}$ (normalizing factors are from Barrat et al. 2012) is between 4.56 – 5.22 for AZ chevkinites and between 2.48 – 2.67 for PAK chevkinites, suggesting that the former crystallized from a more differentiated melt than the latter. Ti, Zr, and Nb contents are quite different between AZ and PAK chevkinite: Ti 2.28 – 2.62 vs. 2.58 – 2.69, Zr 0.03 – 0.13 vs. 0.01, and Nb 0.20 – 0.37 vs. 0.04 apfu, respectively. Total Fe is 1.69 – 2.00 apfu in AZ ($Fe^{3+}/\Sigma Fe = 0.24$), 1.96 – 2.10 apfu in PAK ($Fe^{3+}/\Sigma Fe = 0.48$). The Mg content is generally higher in PAK (0.10 apfu) than in AZ (≤0.06 apfu), the only exception being the ID crystal from the AZ samples (0.12 apfu). The Mn range is similar in AZ and PAK, 0.06 – 0.11 and 0.06 – 0.13 apfu, respectively. The Al content is 0.01 – 0.07 in AZ and 0.02 – 0.05 apfu in PAK. Minor elements include Th (0.05 – 0.08, 0.03 – 0.04 apfu in PAK and AZ, respectively), Sr (0.03 – 0.04 apfu in PAK), and Y (0.02 – 0.03 apfu) in AZ.

Possible degrees of associations among elements were investigated for all point analyses (n=131 for AZ and n=29 for PAK crystals); the correlation matrix obtained allowed the identification of the elements that are most highly correlated. In AZ chevkinites, the wide Ca-REE range and the significant Zr and Nb concentrations revealed strong positive correlations among Ca, Ti, and Zr, and negative among REE, Fe^{2+}, and Nb (Fig 5a), thus suggesting a substitution mechanism such as **(**Ca+Ti+Zr**)** ↔ **(**REE+Fe^{2+}+Nb). In this substitution, all octahedral, and not only the C sites, are involved (Green and Pearson 1988). The refined site occupancies (see XRD section) indicate that Ti is disordered among the C and D sites and Fe among the B, C, and D sites (e.g., Calvo and Faggiani 1974; Sokolova et al. 2004; Yang et al. 2008; Stachowicz et al. 2019b; Nagashima et al. 2020). These findings disagree with the general equation of substitution mechanism $(Ca^{2+}+Sr^{2+})_A+(Ti^{4+}+Zr)_C \leftrightarrow [(REE,Y)^{3+}]_A+(M^{2+,3+})_C$ proposed by McDowell (1979), Parodi et al. (1994), Della Ventura et al. (2001), Macdonald and Belkin (2002), and Vlach and Gualda (2007), where only A and C sites are taken into account.

HFSE elements, such as Nb and Zr, play a crucial role for charge balancing substitutions. A negative correlation exists between Zr and Nb (correlation coefficient: ca. -0.74) (Fig. 5b) and at high Nb and low Zr (or Ca) contents, the compositional variability of the patchy zoned crystals is evident. Moreover, considering the Nb mineral/bulk rock partitioning, the Nb content is much higher in the AZ chevkinite (2.14 – 3.89 wt% Nb_2O_5; Table 1) than in its host rock (up to 350 ppm; Ridolfi et al. 2003) as previously reported by Macdonald et al. (2002) for two Kenyan samples. The diagram in Figure S2 displays the partitioning of Nb between chevkinite and the host rock for several literature localities, showing how Nb content in chevkinite increases proportionally to the amount of Nb in the system. In the LdF5 chevkinite, other octahedral cations such as Mg and Al, are positively correlated with Ti and Zr and negatively with Fe^{2+} and Nb. A possible substitution at the octahedral sites is (Ti+Zr+Mg+Al) ↔ (Fe^{2+}+Nb+Mn).

In PAK chevkinites, a substitution of the type (Ca+Th) ↔ (2REE) is recognizable in crystals 6 and 7, Ca being negatively correlated with Ce (correlation coefficient: ca. -0.72) and Nd. In addition, exchange reactions involving both A and the octahedral sites are (Ca+Zr+Th) ↔ (2REE+Fe^{2+}+Mn) or (Ca+Zr+Th) ↔ (2REE+Ti), Ca being positively correlated with Zr (correlation coefficient: 0.57), and negatively correlated with Fe^{2+}, Mn, and Ti. Conversely, no Ca-REE compositional zoning is found in crystal 4, which has the highest Fe_{tot} and Mg, lowest Ti and Mn contents, and the highest Fe^{3+}/Fe_{tot} ratio (ca. 0.50). The most significant substitution therefore occurs only at the octahedral sites, i.e., (Fe^{3+}+Mg+Al) ↔ (Fe^{2+}+Ti+Mn), Fe^{3+} being positively correlated with Mg and Al and negatively with Fe^{2+}, Ti, and Mn. This substitution is also valid for crystals 6 and 7.

Transmission electron microscopy (TEM)

TEM data analysis confirmed the non-metamict nature of both PAK and AZ chevkinites. In all of the SAED patterns, there are only sharp and bright diffraction spots, indicative of the high crystallinity at both the sub-micrometer and reticular planes scales of all the chevkinite micro-grains studied. The SAED patterns along the [010] direction (*b* axis), i.e., perpendicular to the structural layer stacking direction, did not show streaked spots (as shown in Fig. 6), which indicates the regularity of the layer alternation. Along this direction, neither weak diffraction spots nor spots due to multiple scattering were observed. HRTEM images also showed similar structural regularity in all samples, further confirming that they are non-metamict (Fig. S3). No simulations of structural image were performed to compare with the obtained HRTEM images in order to propose structural models. For any examined crystallographic direction, the comparison between the crystallographic planes obtained by the indexed SAED patterns with the sides of the micro-grains (both at medium and high magnification) has highlighted no preferential direction of fracturing. This is evident in Appendix B (Table 1B), where the frequency of the crystallographic directions of the various edges is indicated.

Crystal structure refinement (XRD)

After data collection carried out on the same chevkinite crystals chemically investigated through EMPA, intensities were corrected for Lorentz and polarization effects, and the absorption correction calculated using optimized shape (X-SHAPE, STOE 1999). Space group determination, performed with the software GRAL (CrysAlis 17128.c4), indicates $P2_1/a$ space group for both AZ and PAK chevkinites. More specifically, we checked reflections for two representative samples, AZ 74 and PAK 7 (Table S3); inspection of the $I/\sigma(I) > 4$ reflections allowed us to establish that for $h + k = 2n$ reflections in comparison with $h + k = 2n +1$ reflections:

- $N_{4\sigma}$, the number of reflections exceeding the 4σ level, is definitely higher;
- the average intensity is at least ten times higher.

Therefore, the $h + k = 2n$ reflections are systematically stronger, sharper, and more accurate than the reflections with $h + k = 2n + 1$, as previously observed in matsubaraite (Miyajima et al. 2002), rengeite (Miyawaki et al. 2002), and Ti- and Fe^{2+}-rich chevkinite-(Ce) (Li et al. 2005). In terms of group-subgroup relations, in perrierite and chevkinite, the $P2_1/a$ structure can be regarded as a distortion derivative (pseudo-$C2/m$) of the parent $C2/m$ structure since the deviations of the atomic coordinates from the corresponding positions in the $C2/m$ model are generally small; the $h + k = 2n + 1$ reflections are weak because the deviations from C-centering are small. Performing least square refinements keeping only the $h + k = 2n$ reflections and cutting off the $h + k = 2n + 1$ reflections yields the $C2/m$ space group. The results of least square refinements obtained in the $C2/m$ and $P2_1/a$ space groups are both very good and shown in Table S4 for the two representative samples AZ 74 and PAK 7. The adopted refinement strategies will be reported later in this section. Between the two structures, the number of electrons per site and the total number of electrons generally differ by less than 1%. Tables S5 and S6 show the deviations of the atomic coordinates in the $P2_1/a$ structure from the corresponding positions in the *C*2/*m* structure (maximum 0.002-0.003 in the *x* coordinate of the C1 site, ~ 0.02 in the *y* coordinate of the A2, O6, O7 sites, and ~ 0.01 in the *y* coordinate of A1 and O3(1) sites). Transformation occurs by the suppression of mirror planes at *y* = 0 and *y* = 0.5 such that there are more atoms in the asymmetric unit of the transformed crystal structure (Li et al. 2005; Stachowicz et al. 2019b). The O1, O2, and O3 sites in the *C*2/*m* model are divided into two sites in the $P2_1/a$ model: O1 and O1(1); O2 and O2(1); O3 and O3(1), respectively, related by pseudo-mirror planes at *y* = 0 and *y* = 0.5. The A1, A2, Si1, and Si2 sites and the O4, O5, O6, O7, and O8 oxygen atoms are released from the mirror plane, gaining an additional degree of freedom. In Tables S7 and S8, reporting the polyhedral bond lengths in the *C*2/*m* and $P2_1/a$ structures, the values of the respective mean bond lengths in the B, C1, C2A, and C2B octahedral sites differ within one estimated standard deviation.

On comparing the *C*2/*m* structure of perrierite-(Ce) with the distorted $P2_1/a$ structure of synthetic perrierite $La_4Mg_2Ti_3O_8(Si_2O_7)_2$, Malcherek et al. (2021; their Fig. 6) have shown that the displacement ellipsoids obtained for the *C*2/*m* structure at room temperature encompass the atom positions of the distorted $P2_1/a$ structure at the 95% probability level. This indicates that the distortions present in the $P2_1/a$ structure are locally present as domains within the *C*2/*m* structure. The observed *C*2/*m* structure is the result of averaging over many such domains with different senses of distortion. Similarly, the displacement parameters in the two samples AZ 74 and PAK 7, refined both in the *C*2/*m* and in the $P2_1/a$ space groups, are larger in the former than in the latter space group (CIF file; see also Stachowicz et al. 2019b); in the average *C*2/*m* structure the displacement parameters increase to accommodate the static atomic displacements of the actual, distorted crystal structure. We will use the average *C*2/*m* structure for further interpretation of our data. Table 3 shows the refinements carried out against F_o^2 through 2Θ = 60° in space group *C*2/*m* for all of the samples using the SHELX97 program (Sheldrick 1997). No chemical constraints were imposed on the refinements. Refined parameters were scale factors, atomic coordinates, displacement parameters (first isotropic and then anisotropic), and the occupancies at the A, B, C1, C2A, and C2B sites. To avoid undesirable correlations among variables, specific refinement strategies were implemented for a total of 106 parameters varying together. A final difference-Fourier map showed only peaks less than 1 e^{-} $Å^{-3}$. The rms fluctuation of the map relative to the mean density was less than ~ 0.2 e^{-} $Å^{-3}$. When two scattering curves were assigned to sites involved in isomorphous replacement, constraints of full site occupancy and equal displacement parameters were imposed. The best *Fo–Fc* agreement was obtained by selecting the most consistent scattering curves. For tetrahedral cations and O anions, where solid solution does not occur, neutral versus ionized scattering curves and partially ionized scattering curves were used, respectively (Ungaretti et al. 1983; Merli et al. 2000), i.e., a 0.625 occupancy of Si^{+4} against 0.375 of Si for the T sites and a 0.50 occupancy of O^{-1} against a 0.50 occupancy of O^{-2} for the O sites. Scattering factors were taken from Wilson (1992) and from Tokonami (1965) for O^{-2}. For the A, B, C1, C2A, and C2B sites fully ionized scattering curves were used. Initially, only Ce^{3+} at both A sites, Fe^{2+} at the B site and Ti^{4+} at the C1, C2A, and C2B sites were assigned. However, the refinements showed that Ce occupancy was always < 1, Fe occupancy was usually < 1 in PAK chevkinite and ca. 1 or slightly greater in AZ chevkinite, and Ti occupancies were always slightly greater or well over 1. The scattering curves of Ce^{3+} and Ca^{2+} were then used for the A sites. For the B site, the scattering curves of Fe^{2+} and Mg^{2+} were used in PAK chevkinite, and only the curve of Fe^{2+} was used in AZ chevkinite, while its occupancy was not constrained to 1. For the C1, C2A, and C2B sites, either the scattering curves of Ti^{4+} and Fe^{2+} were used or, when Ti occupancy resulted well over 1, those of Ti^{4+} and Nb^{5+}. As pointed out by Dollase (1971), the scattering curves are assumed to approximate the true number of electrons (ne^{-}) per site. The range of ne^{-} is 51.54 – 55.07 (A1), 49.56 – 53.86 (A2). Thus, heavier cations are expected at the A1 site. Moreover, these two sites can be assumed to be filled by a mixture of Ca and REE, rather than

REE alone. At the B site, the ne$^-$ value is near to or slightly higher than 26 in AZ chevkinite, whereas it is significantly lower (24.6) in PAK chevkinite. At the C1 site, the ne$^-$ in AZ (ca. 23.4) and PAK (ca. 23.8) chevkinites is similar, indicating the presence of heavier cations, such as Fe, together with Ti^{4+}. Conversely, compared to C1, the ne$^-$ values of both C2A and C2B sites are higher in AZ chevkinite (range: ca. 24 – 28), implying the presence of substitutes heavier than Fe (e.g., Nb), and lower in PAK chevkinite (ca. 22 – 23), suggesting a higher Ti^{4+} occupancy. The highest atomic displacement parameters (ADP) are shown by O7, the bridging oxygen in the Si_2O_7 group (CIF files). Significantly high ADP values are also shown by O6, the most undersaturated oxygen in the structure, and by O3. For the cations, the highest ADP value is shown by the A2 site.

In Table 3, the total ne$^-$ calculated from site occupancy refinement (ne$^-_{ref.}$) and the total ne$^-$ determined from average microprobe analysis on the same crystal (ne$^-_{chem.}$), together with respective estimated errors, are reported (see Appendix A for definition of errors). In crystal 9, the ne$^-_{chem.}$ value is affected by the largest estimated error due to strong Ca-REE compositional variations. Nevertheless, its agreement with ne$^-_{ref.}$ is satisfactory.

Cation distribution

Table 4 reports the calculated cation distributions. For some representative samples, the calculated and expected values and relative errors are reported in Table S2.

The cation distribution at the A1 and A2 sites, although based only on the number of electrons, is consistent with a model where site preference is a function of the rare earth ionic size. According to this model, La enters only the higher-coordinated A2 site, whereas the heavier and smaller REE, Pr, Nd, Sm, and Gd, would enter only the 8-coordinated A1 site. Ce, intermediate in size compared to the above cations, can enter both the A2 and A1 sites. Most notably, the ionic radii of Pr, Nd, Sm, and Gd, given their site preference (e.g., coordination number 8 or 9), have never been determined for a coordination number 10 (Shannon 1976), and no evidence for these larger polyhedra to be occupied by smaller Y-group rare earths (from Gd to Lu) has ever been reported (Miyawaki and Nakai 1996). Similarly, the non-REE cations are also distributed between sites depending on their size: Ca, in light of its similarity with Ce, enters both the 10- and 8-coordinated sites; Sr, even bigger than La, enters only the 10-coordinated A2 site and Th, close in size to Gd, enters only the 8-coordinated A1site. After optimization of the site assignment, PAK and AZ samples exhibit distinct REE proportions; for instance, Ce ions are more abundant than La at the A2 site in PAK samples, less in AZ. The A1 site is Nd- and Pr-richer in PAK samples than in AZ.

In all samples, the B site is predominantly occupied by Fe^{2+}. There are, however, some significant substitutions. Mg is mainly found at the B site in all PAK samples (ca. 0.08 apfu), as well as in the 4A and 4GR AZ samples (ca. 0.04 apfu). Ca is found with small to significant quantities (up to 0.09 apfu) not only in Ca- and Zr-rich (ID, 45, 11, and 44 hosted in LdF5 syenite) but also in Ca-poor AZ samples characterized by patchy zoning (9 and 74 hosted in LdF1 syenite). In the Ca- and Zr-rich samples, Zr^{4+} enters the B site with up to 0.075 apfu, which represents more than 80% of the total Zr cations.

At the C1 site of PAK samples the most important substitutions are those involving Ti and Fe^{3+}. Where the Fe^{3+}/Fe_{tot} ratio is highest, Fe^{3+} is dominant over Ti (e.g., sample 4). On the other hand, in AZ samples, Ti occupies between 56 and 58% of the C1 site, the remainder being a mixture of both Fe^{2+} and Fe^{3+}.

The C2A and C2B sites of PAK samples are dominated by Ti, filling 80% and 90% of these sites, respectively; the remainder is mainly Fe^{2+}. Conversely, in AZ samples, Ti competes with substituting Fe, Nb, Zr, and Mg, its occupancy being as low as 50% at the C2B site. Nb is mainly disordered between the C2A and C2B sites, while in the Ca- and Zr-rich samples, it is also present at the C1 site, although always in small quantities only. Zr is ordered at the C2A site except in the Ca-and Zr-rich samples, where it is disordered between B and C2A sites.

To compare our cation distribution with previous studies, we report some insights from the literature based mainly on site occupancy refinements. However, a comprehensive presentation of cation distribution in chevkinites and perrierites is found in the review by Macdonald et al. (2019). In the chevkinite samples studied by Yang et al. (2002), Li et al. (2005), Holtstam et al. (2017), Stachowicz et al. (2019b), and Nagashima et al. (2020), the refined site occupancy values at the non-equivalent A1 and A2 sites showed the number of electrons at the A1 site to be greater than at A2, suggesting a non-uniform distribution of REE and Ca between the two sites. In the chevkinite samples studied by Nagashima et al. (2020), a higher occupancy of Ca is proposed at the A2 site than at A1 and vice versa for Ce. McDowell (1979), based on a microprobe study of CGM from California, suggested that Ca substituted only for the larger and lighter REE, La and Ce, and the extent of REE-Ca substitution decreased with a decrease in ionic radius through lanthanide contraction. Furthermore, ionic radii data should suggest that smaller and heavier REE occupy the lower-coordinated A1 site and Ca substitutes for the larger REE at the higher-coordinated A2 site. In the samples studied by Sokolova et al. (2004), Fe is the dominant cation at the B site (85 – 93%), mainly as Fe^{2+}, although the presence of Fe^{3+} could not be excluded due to a particularly short value of the <B-O> mean bond length. Nagashima et al. (2020) proposed the dominant iron valence to be ferric in the Haramosh sample, and ferrous in the Ashizuri and the Tangir samples. Previous studies on chevkinites showed that the C1 sites are dominated by either Ti^{4+} or Fe^{3+}. Fe^{3+} is the most abundant cation in sample (2^{an}) (Sokolova et al. 2004) and in delhuyarite-(Ce) (Holtstam et al. 2017), the former with a significant amount of Ti^{4+}, the latter with W^{6+}. Although Ti^{4+} is the dominant cation at the C2A and C2B sites, replacements of tetravalent by pentavalent ions were predicted as favorable by Calvo and Faggiani (1974) on the basis of a charge distribution study (calculated charge for the C2A and C2B sites = +4.14).

Geometry of coordination polyhedra

Polyhedral bond lengths, volumes and distortion parameters are reported in Table 5. To describe polyhedral distortions, the octahedral $\sigma^2_{\theta\ (\mathrm{oct})}$ and tetrahedral $\sigma^2_{\theta\ (\mathrm{tet})}$ angle variances (Robinson et al. 1971) are used. In addition, since each bond length is affected by a different estimated error, weighted averages of the bond distances at both octahedral and tetrahedral sites are also reported (see Appendix A for the relative formula and estimated standard deviation).

Volumes and <Si-O> mean values in the Si1 and Si2 tetrahedra are rather similar due to the full occupancy of Si^{4+}. While the Si1 tetrahedron is extremely regular (sharing only corners with nearby polyhedra), the Si2 tetrahedron is much more distorted because it shares the O3-O3 edge with the large and highly charged A2 polyhedron (Fig. 7). The B site is the largest and the most distorted octahedron in the structure, its angle variance varying proportionally to its size. In the rutile-like layer formed by the two distinct C1-C1 and C2A-C2B chains (Fig. 1), the C1 site is more distorted and the smallest octahedron with the shortest shared edge between the C1 cations. The C2A and C2B sites are low-distortion polyhedra; the C2A site is always larger than C2B, favoring significant substitution of Ti^{4+} by larger cations (e.g., Fe^{2+}).

In the 8-coordinated A1 site, the range in the interatomic distances is between 2.474 and 2.864 Å in AZ, 2.488 – 2.849 Å in PAK chevkinites (Table 5). In all crystals, the mean of the eight bond lengths <A1-O> is between 2.558 and 2.562 Å. The A1-O7 and A1-O6 distances, both around 3.2 Å, are not included in the calculation of the mean value but are taken into account in the calculation of the bond valence sums (BVS) (see Discussion). In the 10-coordinated A2 site, the range in the interatomic distances between AZ and PAK chevkinites is quite similar and equal to 2.410 – 2.984 Å and 2.412 –

2.987 Å, respectively. The two A2-O6 distances between 2.980 and 2.987 Å are much longer than the average bond length (2.654-2.658 Å), making the polyhedron very irregular; however, they are just below 3Å, a reasonable limit for a bond to exist (Brown 2002). Moreover, in the AZ samples 75, 74, and 9 the A2-O3 distances are shorter than the A2-O1. Comparison of the A2-O3 and the A2-O1 values shows that, going from Ca-rich to Ca-poor samples, a decrease of the A2-O3 distances from 2.633 to 2.609 Å corresponds to a proportional increase of the A2-O1 distances. Inspection of the atomic coordinates shows that the shortening of A2-O3 is achieved through a shift of A2 away from O1 and towards O3 mainly along the *c* axis, and through a shift of O3 towards A2 along the *b* axis (Fig. 7). Consequently, the A2-Si2 cation-cation distance and the length of the O3-O3 edge in common between the A2 and the Si2 polyhedra also decrease (Table 5). The shortest A2-Si2 (i.e., 3.221 Å) and O3-O3 edge (2.594 Å) distances are found in sample 9. Furthermore, the shortening of the A2-O3 bond lengths appears closely associated with the lengthening of the respective B-O3 distances (Fig. 7) and of the B overall size, the highest <B-O> mean value (2.162 Å) and greatest distortion ($\sigma^2_{\theta\,(oct)}$ = 117.5) occurring in sample 9. In the PAK samples, the size of C1 is small, indicating only substitution of Ti^{4+} by Fe^{3+} (<C1-O> in the range 1.986 – 1.988 Å). In sample 7, the C1 cations also face the shortest shared edge (O4-O5 = 2.675 Å) in the whole rutile-like layer. Conversely, in the AZ samples the C1 size tends to increase as Fe^{2+} exceeds Fe^{3+}in substitution of Ti^{4+}. However, since C1 does not easily adapt to the entry of large cations, only a slight increase of <C1-O> of up to 1.993 Å is observed compared to a remarkably longer calculated value of 2.027 Å (sample 9 in Table S2). In the same way, a slight increase occurs of $\sigma^2_{\theta\,(oct)}$, up to 15.2. An increase of <C2A-O> and, to a lesser extent, of <C2B-O> is also associated with the increase of <C1-O> (cf. sample 9).

Finally, the role of Zr^{4+} entering the B site in the Ca-rich AZ samples (ID, 45,11, 44), should be emphasized. Unlike the Ca-poor samples, in the Ca-rich samples, the B-O3 distances are shorter and the difference between the B-O3 and the B-O6 bond lengths is also smaller. As a result, overall site distortion is also smaller (e.g., $\sigma^2_{\theta\ (oct)}$ = 104.6 in sample ID).

Mössbauer

The 11K MS spectrum, reported in Fig. 8, consists of two strong and broad absorptions at low velocity together with a third one at high velocity, indicating the superimposition of several ferric and ferrous contributions. The best fitting model was obtained using three doublets: one ascribable to Fe(III), Db1, and two assigned to Fe(II), Db2 and Db3. The obtained hyperfine parameters, reported in Table 6, are representative of distorted octahedral sites. The oxidation ratio, expressed as [Fe(III)/Fe(III)+Fe(II)] (Macdonald et al. 2019), is close to 0.55. Db1, characterized by a broad linewidth, shows δ and Δ values unambiguously attributable to a sixfold Fe(III) hosted in a distorted site. The rather high Γ value suggests the superimposition of different ferric sites, but every attempt to split the ferric component into different doublets leads to unsatisfactory results. The presence of only one crystallographic site populated by Fe(III) seems in contrast with previous studies where R*T* (Song et al. 1999; Yang et al. 2007; Nagashima et al. 2020) or 80K (Li et al. 1992) MS analyses of non-metamict chevkinites showed ferric ions occupying two different crystallographic sites. Based on the four-components fitting outcome, it is proposed here that ferric ions occupy a single site, and the line broadening is associated to the high substitution degree in the next nearest neighbors. An additional fitting by Quadrupole Splitting Distribution (QDS) was also attempted. The outcome, showing a slightly asymmetric distribution on the ferric site, and an unconvincingly bimodal one for the ferrous sites, was not judged conclusive in describing the Fe distribution.

The two ferrous doublets Db2 and Db3 are characterized by different Δ values as a result of non-ideal site geometry, different Fe-O bond distances, and the distribution and nature of the next nearest neighbors. Db2, showing the highest Δ value, should be representative of a small and less distorted octahedral site, while Db3 of a highly distorted site. This is in agreement with the literature data (Li et al. 1992; Song et al. 1999; Yang et al. 2007; Nagashima et al. 2020) and the structural topology.

DISCUSSION

Strain in bonds

Table 7 reports the bond valence sums (BVS) calculated with the proposed cation distribution using equation (2) of Bosi (2014) and the corresponding formal valences for some representative samples (AZ 44, AZ 9 and PAK 4). BVS values in AZ samples approximate the corresponding formal anion charges better than in PAK, mainly due to higher contributions to the most undercharged O6 and O3 oxygens from the cation sites and to the O5 oxygen from the C2A site (i.e., from Nb^{5+}). Furthermore, the O6 oxygen atom in sample 44 is better balanced than in sample 9 because of the highest contributions from Y, Ca and Zr in the B site (Table 4). The O3 BVS values in samples 44 and 9 are similar (1.94 and 1.95, respectively), and much closer to the oxygen formal charge than in the PAK sample (1.89). These values, however, are the result of opposite contributions from the A and the B sites: in sample 44, we see the concurrent lengthening of A2-O3 and shortening of B-O3 bond distances, and the opposite in sample 9. Therefore, the undercharged O6 and O3 oxygens might act as a flex point. As for cations, calculated BVS values are significantly lower than the respective formal charges for the A1 and C2A sites, while they are higher for the Si1 and Si2 sites due to the distinct nature of the strong Si-O bonds. Most remarkable is the discrepancy for the A1 site; even considering the distances A1-O6 and A1-O7 of ca. 3.2 Å (Table 5), each yielding ~ 0.05 bond valence units, calculated BVS' values (Table 7) are still significantly lower than the corresponding formal valences. Thus, the A1 site with its rather long bond lengths would not seem suitable to accommodate the smaller sized LREE, praseodymium, neodymium, samarium, and even less, the smallest REE gadolinium to lutetium if present. Finally, the unusual increase of the BVS value should be noted because it is well over its formal charge at the B site in sample 44 (Table 7); the entry of small amounts of Y^{3+} and Zr^{4+}, together with Ca^{2+} in place of Fe^{2+}, actually increases the formal charge at the B site with respect to other samples. In addition, the unusually high BVS value is due to short B-O bond lengths (Table 5) and to high values of bond valence parameters for Y^{3+}, Ca^{2+}, and Zr^{4+} cations (Brese and O'Keeffe 1991). Since the discrepancy between formal charge and BVS value at the B site is among the highest ever calculated, the Ca- and Zr-rich samples investigated in this work might represent compositional end-members for the chevkinite structure. Taking into account the global instability index (GII) (Salinas-Sanchez et al. 1992), the calculated values for AZ and PAK chevkinites (all in the range 0.11 – 0.12 valence units, vu) suggest a slightly strained structure (Brown 2002). Notably, the GII index for synthetic chevkinite (Calvo and Faggiani 1974) returned the same value (0.11 vu), suggesting it is intrinsic of this structure.

Valence state and coordination number of Fe ions in Pak chevkinite

To check the oxidation state and coordination number of Fe ions in PAK chevkinites, the results obtained from Mössbauer spectroscopy and from cation distribution were compared. However, before comparing results, it is worth summarizing some important differences between these two independent analysis techniques. While Mössbauer spectroscopy was carried out on a large number of crystals of the sample, X-ray structure refinement was performed on just one fragment per sample. Moreover, whereas site occupancy derived from structure refinement is averaged over a huge number of crystallographic sites, a Mössbauer spectrum is the result of the sum of contributions of each iron nucleus and whenever these contributions can be separated in the spectral deconvolution, it can provide information about oxidation state and site geometry of each nucleus. From the crystal chemical viewpoint, the Fe^{2+} and Fe^{3+} cation fractions selected for comparison are those calculated by the minimization procedure, representing 8 of the 49 variable parameters used. The results obtained with the two methodologies are summarized in Table 8. The only Fe^{3+}component determined by Mössbauer spectroscopy (A = 55 ± 4%) is identifiable occupying the site C1 in the chevkinite structure. On the other hand, Fe^{3+} obtained in the minimization procedure is in the range 45 – 50% with a preponderant distribution at the C1 site (44 – 48%) plus a small quantity at the C2B site (1 – 2%). No Fe^{3+} was assigned to the largest and most distorted octahedral B site by either Mössbauer spectroscopy or minimization. The Fe^{2+} component (A = 35 ± 3%) with the highest isomeric shift value is Fe^{2+} entering the most distorted crystallographic site B. In the three single crystals studied, Fe^{2+} at the B site is calculated between 39 – 41%. The other Fe^{2+} component in the Mössbauer analysis (A = 10 ± 1%), representative of a less distorted octahedral site, corresponds to Fe^{2+} distributed between the C2A (8 – 9%) and C1 and C2B sites (2 – 4%).

Comparison with partly metamict samples

Values of <B-O> mean bond length vs. cell volume from this work have been compared with previous studies on non-metamict and partly metamict chevkinites (Fig. 9). In non-metamict chevkinites, cell volumes are generally smaller than in metamict chevkinites, and the range of the <B-O> values is between ca. 2.13 and just over 2.16 Å (Yang et al. 2002; Li et al. 2005; Nagashima et al. 2020; this study). In contrast, partly metamict chevkinites can have <B-O> values either shorter, 2.10 – 2.11 Å (Stachowicz et al. 2019a, 2019b), or longer, > 2.16 Å (Sokolova et al. 2004), than non-metamict samples. This suggests that the <B-O> values in the site B could be used to identify different metamict states occurring in chevkinite. However, it is still unsure which types of defects are present in the chevkinite structure. Based on structure refinement of partly metamict chevkinites, it appears that the geometry of the B site is the most sensitive to structural changes, as previously observed during annealing of damaged structures (Sokolova et al. 2004) and in the $C2/m \rightarrow P2_1/a$ transformation (Stachowicz et al. 2019b). In these samples, the A1 and A2 bond lengths connecting the A sites to the B site through the O3 oxygen are unusually large (Stachowicz et al. 2019b, their Table S1; Sokolova et al. 2004, their Table 4), suggesting the onset of structural defects during metamictization. Leaching of REE cations from the chevkinite framework with the consequent loss of stoichiometry in the mineral formula has been extensively shown to happen in chevkinite as a result of hydrothermal alteration (Macdonald et al. 2017; and references therein). However, more work and additional data, particularly at the micrometer- to sub-micrometer-scale, are needed to better understand these complex phenomena.

IMPLICATIONS

Crystal chemical studies help better understand the well-known ability of chevkinite to fractionate LREE from HREE and its importance in geochemical modeling (Macdonald and Belkin 2002). This study showed that at the A1 and A2 sites, the cation distribution is consistent with a model where site preference is a function of the rare earth ionic size. Similarly, the non-REE cations at the A sites are also found distributed depending on their size. Heavier and smaller REE enter only the 8-coordinated A1 site; however, a comparison between BVS and formal charge identifies particularly stretched bonds, suggesting that the A1 polyhedron bond lengths are still too long for HREE.

In the Azores chevkinites, a substitution mechanism of the type **(**Ca+Ti+Zr**)** ↔ **(**REE+Fe^{2+}+Nb) is recognized, as a result of the wide Ca-REE range and the significant Zr and Nb concentrations. Possible structural stability limits of chevkinites with either high-Ca (Ti and Zr) or low-Ca (high REE, Fe^{2+} and Nb) contents are identified, associated with the occupants of the B site in the former and of the C1 sites in the latter. When the availability of REE and Ca is high during chevkinite growth, Ca in excess at the A sites is forced, together with Zr, to enter the B site (Segalstad and Larsen 1978; Platt et al. 1987). From the crystal chemical perspective, a significant increase of the BVS with respect to the formal valence might represent the limit beyond which Ca-richer compositions are no longer stable. In the structure of the most REE- and Fe^{2+}-rich chevkinite, small amounts of Ca are also forced to enter the B site, in which case Fe^{2+} in excess at the B site must enter the C1 sites, thus prevailing over Fe^{3+} in substitution of Ti^{4+}. However, the C1 sites do not easily accommodate significant amounts of large cations raising doubts about any possible additional increase of their Fe^{2+} content. Moreover, in the structure of the chevkinite most enriched in REE- and Fe^{2+}, a distinct configuration around the O3 oxygen results in a better balance of one of the most underbonded anions.

In the Pakistan chevkinite, the low contents of Nb^{5+} and Zr^{4+} clearly affect the underbonding of the O3 and O6 oxygens. The Fe^{3+}/Fe_{tot} ratio (0.50) is the highest among the samples studied; notably, the presence of Fe^{3+} at the B site is neither calculated in the minimization procedure nor observed by Mössbauer spectral analysis.

Chevkinite-(Ce), like only few other minerals, is a Ti silicate where chains of Ti, called C and D in the general formula, form a layer (layer silicates: Sokolova and Hawthorne 2004). This study showed that the D as well as C chains are not always dominated by Ti. Therefore, when describing compositional variations through exchange reactions of the type $(Ca^{2+}+Sr^{2+})_A+(Ti^{4+}+Zr)_C \leftrightarrow [(REE,Y)^{3+}]_A+(M^{2+,3+})_C$ (e.g., Vlach and Gualda 2007), Ti disorder is better described considering both C and D sites.

Similar to many other accessory minerals, complex zoning in chevkinite may also be the result of secondary processes such as deuteric/hydrothermal alteration. Crystal-chemical and structural studies on non-metamict chevkinite from the Azores were instrumental in establishing that crystallinity is not affected by chemical alteration. This is in agreement with the findings of a previous study by Harlov et al. (2011) focusing on the crystallinity of experimentally altered monazite.

ACKNOWLEDGMENTS

The authors thank CNR-IGG for the maintenance of the electron microprobe laboratory in Padova. S.C. greatly acknowledges the expertise of Giorgio Menegazzo who wrote the minimization program and tested it with no regard of time. Anna Fioretti, Ferdinando Bosi, Ray Macdonald, Marcin Stachowicz, Francesco Princivalle, and Silvano Sommacal are warmly thanked for their help in various aspects that led to the development of this work. Renato Pagano and the late Vittorio Mattioli kindly provided the Pakistan chevkinite sample investigated in the present study. The authors are also very grateful to Federico Pezzotta (Museo di Storia Naturale, Milano, Italy) and to Umberto Righi, an Italian mineral collector, for the information given about the outcrop of the chevkinite host-rock along the Tangir Valley in north-western Pakistan. We thank Raul Carampin (CNR-IGG, Padova) for his generous assistance with the microprobe analysis, and Sandra Boesso for heavy liquid concentrations of chevkinite minerals. Nikita Chukanov, an anonymous reviewer, and Lee Groat provided very detailed and helpful reviews of the manuscript. Editorial handling by Charles Geiger is gratefully acknowledged.

REFERENCES CITED

Angel, R.J., Allan, D.R., Miletich, R., and Finger, L.W. (1997) The use of quartz as an internal pressure standard in high-pressure crystallography. Journal of Applied Crystallography, 30, 461-466.

Angel, R.J., Downs, R.T., and Finger, L.W. (2000) High-temperature-high-pressure diffractometry. Reviews in Mineralogy and Geochemistry, 41, 559-596.

Barrat, J.A., Zanda, B., Moynier, F., Bollinger, C., Liorzou, C., and Bayon, G. (2012) Geochemistry of CI chondrites: Major and trace elements, and Cu and Zn isotopes. Geochimica et Cosmochimica Acta, 83, 79-92.

Belkin, H.E., Macdonald, R., and Grew, E.S. (2009) Chevkinite-group minerals from granulite-facies metamorphic rocks and associated pegmatites of East Antarctica and South India. Mineralogical Magazine, 73, 149-164.

Bonatti, S. (1959) Chevkinite, perrierite and epidotes. American Mineralogist, 44,115-137.

Bonatti, S., and Gottardi, G. (1966) Un caso di polimorfismo a strati in sorosilicati: perrierite e chevkinite. Periodico di Mineralogia, 35, 69-91.

Bosi, F. (2014) Bond valence at mixed occupancy sites. I Regular polyhedra. Acta Crystallographica, B70, 864-870.

Boudias, C., and Monceau, D. (1998) Ca.R.Ine Crystallography 3-1 for Microsoft Windows- User manual. Senlis, France.

Brese, N.E., and O’Keeffe, M. (1991) Bond-valence parameters for solids. Acta Crystallographica, B47, 192-197.

Brown, I.D. (1981) The bond-valence method. An empirical approach to chemical structure and bonding. In M. O’Keeffe and A. Navrotsky, Eds., Structure and Bonding in Crystals, p. 1-52, Vol. 2, Academic Press, New York.

Brown, I.D. (2002) The chemical Bond in Inorganic Chemistry: The Bond Valence Model, 278 p. Oxford University Press, New York.

Calvo, C., and Faggiani, R. (1974) A re-investigation of the crystal structures of chevkinite and perrierite. American Mineralogist, 59, 1277-1285.

Carbonin, S., Liziero, F., and Fuso, C. (2005) Mineral chemistry of accessory minerals in alkaline complexes from the Alto Paraguay Province. In P. Comin-Chiaramonti and C.B. Gomes, Eds., Mesozoic to Cenozoic Alkaline Magmatism in the Brazilian Platform, p. 149-158. Editora da Universidade de São Paulo Fapesp, Brazil.

Čech, F., Povondra, P., and Vrăna, S. (1988) Crystal chemistry of a chevkinite from Zambia. Acta Universitatis Carolinae, Geologica, No.2, 181-193.

Cellai, D., Conticelli, S., and Diella, V. (1993) Perrierite-chevkinite in igneous ultrapotassic rocks from Central Italy: chemical data and their petrologic significance. Periodico di Mineralogia, 62, 57-66.

Chukanov, N.V., Aksenov, S.M., Rastsvetaeva, R.K., Belakovskiy, D.Y., Göttlicher, J., Britvin, S.N., and Möckel, S. (2012) Christofschäferite-(Ce), $(Ce,La,Ca)_4Mn^{2+}(Ti,Fe^{3+})_3(Fe^{3+},Fe^{2+},Ti)(Si_2O_7)_2O_8$, a new chevkinite-group mineral from the Eifel Area, Germany. New data on minerals, 47, 31-40, Moscow.

Della Ventura, G., Williams, C.T., Raudsepp, M., Bellatreccia, F., Caprilli, E., and Giordano, G. (2001) Perrierite-(Ce) and zirconolite from a syenitic ejectum of the Roccamonfina volcano (Latium, Italy): Implications for the mobility of Zr, Ti and REE in volcanic environments. Neues Jahrbuch für Mineralogie, Monatshefte, 9, 385-402.

Dollase, W.A. (1971) Refinement of the crystal structure of epidote, allanite and hancockite. American Mineralogist, 56, 447-464.

Droop, G.T.R. (1987) A general equation for estimating Fe^{3+} concentrations in ferromagnesian silicates and oxides from microprobe analyses, using stoichiometric criteria. Mineralogical Magazine, 51, 431-435.

Ewart, A. (1981) The mineralogy and chemistry of the anorogenic tertiary silicic volcanics of S.E. Queensland and N.E. New South Wales, Australia. Journal of Geophysical Research, 86, B11, 10242-10256.

Exley, R.A. (1980) Microprobe studies of REE-rich accessory minerals: Implications for Skye granite petrogenesis and REE mobility in hydrothermal systems. Earth and Planetary Science Letters, 48, 97-110.

Green, T.H., and Pearson, N.J. (1988) Experimental crystallization of chevkinite/perrierite from REE-enriched silicate liquids at high pressure and temperature. Mineralogical Magazine, 52, 113-120.

Haggerty, S.E., and Mariano, A.N. (1983) Strontian-loparite and strontio-chevkinite: two new minerals in rheomorphic fenites from the Paraná Basin carbonatites, South America. Contributions to Mineralogy and Petrology, 84, 365-381.

Harding, R.R., Merriman, R.J., and Nancarrow, P.H.A. (1982) A note on the occurrence of chevkinite, allanite, and zirkelite on St. Kilda, Scotland. Mineralogical Magazine, 46, 445-448.

Harlov, D. E., Wirth, R., and Hetherington, C. J. (2011) Fluid-mediated partial alteration in monazite: The role of coupled dissolution–reprecipitation in element redistribution and mass transfer. Contribution to Mineralogy and Petrology, 162, 329–348.

Hawthorne, F.C., Ungaretti, L., and Oberti, R. (1995) Site populations in minerals: Terminology and Presentation of results of crystal structure refinement. Canadian Mineralogist, 33, 907–911.

Holtstam, D., Bindi, L., Hålenius, U., and Andersson, U.B. (2017) Delhuyarite-(Ce) – $Ce_4Mg(Fe^{3+}{}_2W)\square(Si_2O_7)_2O_6(OH)_2$ – a new mineral of the chevkinite group, from the Nya Bastnäs Fe-Cu-REE deposit, Sweden. European Journal of Mineralogy, 29, 897-905.

Imaoka, T., and Nakashima, K. (1994) Chevkinite in syenites from cape Ashizuri, Shikoku Island, Japan. Neues Jahrbuch für Mineralogie, Monatshefte, 8, 358-366.

Jaffe, H.W., Evans, H.T. Jr., and Chapman, R.W. (1956) Occurrence and age of chevkinite from devil's slide fayalite-quartz syenite near Stark, New Hampshire. American Mineralogist, 41, 474-487.

Jagoutz, O.E., Müntener, O., Ulmer, P., Pettke, T., Burg, J-P., Dawood, H., and Hussain, S. (2007) Petrology and mineral chemistry of lower crustal intrusions: The Chilas Complex, Kohistan (NW Pakistan). Journal of Petrology, 48, 1895-1953.

Khan, M.A., Jan, M.Q.,Windley, B.F., Tarney, J., and Thirlwall, M.F. (1989) The Chilas mafic-ultramafic igneous complex; The root of the Kohistan island arc in the Himalaya of northern Pakistan. In L.L. Jr. Malinconico and R.J. Lillie, Eds., Tectonics of the Western Himalayas, Special Papers 232, p. 75-94. Geological Society of America, Washington.

King, H.E., and Finger, L.W. (1979) Diffracted beam crystal centering and its application to high pressure crystallography. Journal of Applied Crystallography, 12, 374-378.

Kopylova, M.G., Rickard, R.S., Kleyenstueber, A., Taylor, W.R., Gurney, J.J., and Daniels, L.R.M. (1997) First occurrence of strontian K-Cr-loparite and Cr-chevkinite in diamonds. Russian Geology and Geophysics, 38, 405-420.

Li, Z., Jin, M., Liu, M., and Liu, X. (1992) Iron distribution in chevkinite. Hyperfine Interactions, 70, 1057-1060.

Li, G., Yang, G., Ma, Z., Shi, N., Xiong, M., Fan, H., and Sheng, G. (2005) Crystal structure of natural non-metamict Ti- and Fe^{2+}-rich Chevkinite-(Ce). Acta Geologica Sinica, 79, 325-331.

Lima de Faria, J. (1962) Heat treatment of chevkinite and perrierite. Mineralogical Magazine, 33, 42-47.

Liziero, F. (2008) Studio cristallochimico e strutturale di Chevkiniti-(Ce) non metamittiche, 129 p. Ph.D. thesis, Universita' degli Studi di Padova, Italy.

Macdonald, R., and Belkin, H.E. (2002) Compositional variation in minerals of the chevkinite group. Mineralogical Magazine, 66, 1075-1098.

Macdonald, R., Marshall, A.S., Dawson, J.B., Hinton, R.W., and Hill, P.G. (2002) Chevkinite-group minerals from salic volcanic rocks of the East African Rift. Mineralogical Magazine, 66, 287-299.

Macdonald, R., Belkin, H.E., Wall, F., and Bagiński, B. (2009) Compositional variation in the chevkinite group: new data from igneous and metamorphic rocks. Mineralogical Magazine, 73, 777–796.

Macdonald, R., Bagiński, B., Kartashov, P.M., Zozulya, D., and Dzierżanowski, P. (2012) Chevkinite-group minerals from Russia and Mongolia: new compositional data from metasomatites and ore deposits. Mineralogical Magazine, 76, 535–549.

Macdonald, R., Bagiński, B., Dzierżanowski, P., Fettes, D.J., and Upton, B.G.J. (2013) Chevkinite-group minerals in UK Palaeogene granites: underestimated REE-bearing accessory phases. Canadian Mineralogist, 51, 333-347.

Macdonald, R., Bagiński, B., and Zozulya, D. (2017) Differing responses of zircon, chevkinite-(Ce), monazite-(Ce) and fergusonite-(Y) to hydrothermal alteration: Evidence from the Keivy alkaline province, Kola Peninsula, Russia. Mineralogy and Petrology, 111, 523-545.

Macdonald, R., Bagiński, B., Belkin, H.E., and Stachowicz, M. (2019) Composition, paragenesis, and alteration of the chevkinite group of minerals. American Mineralogist, 104, 348-369.

Malcherek, T., Schlüter, J., and Schäfer, C. (2021) Perrierite-(Ce) from Laacher See tephra, Eifel, Germany, and the modular character of the chevkinite group of minerals. Physics and Chemistry of Minerals, 48, 10.

McDowell, S.D. (1979) Chevkinite from the Little Chief granite porphyry stock, California. American Mineralogist, 64, 721-727.

Merli, M., Ungaretti, L., and Oberti, R. (2000) Leverage analysis and structure refinement of minerals. American Mineralogist, 85, 532-542.

Mitchell, R.S. (1966) Virginia metamict minerals. American Mineralogist, 51, 1394-1405.

Miyajima, H., Miyawaki, R., and Ito, K. (2002) Matsubaraite, $Sr_4Ti_5(Si_2O_7)_2O_8$, a new mineral, the Sr-Ti analogue of perrierite in jadeitite from the Itoigawa-Ohmi district, Niigata Prefecture, Japan. European Journal of Mineralogy, 14, 1119-1128.

Miyawaki, R., and Nakai, I. (1996) Crystal chemical aspects of rare earth minerals. In A.P. Jones, F. Wall and C.T. Williams, Eds., Rare Earth Minerals, p. 21-40. The Mineralogical Society Series, Chapman & Hall, London, U.K.

Miyawaki, R., Matsubara, S., and Miyajima, H. (2002) The crystal structure of rengeite $Sr_4ZrTi_4(Si_2O_7)_2O_8$. Journal of Mineralogical and Petrological Sciences, 97, 7-12.

Moore, R.B. (1991) Geology of three late quaternary stratovolcanoes on São Miguel, Azores. U.S. Geological Survey Bulletin 1900, 46 p.

Muhling, J.R., Suvorova, A.A., and Rasmussen, B. (2014) The occurrence and composition of chevkinite-(Ce) and perrierite-(Ce) in tholeiitic intrusive rocks and lunar mare basalt. American Mineralogist, 99, 1911-1921.

Nagashima, M., Armbruster, T., Akasaka, M., Sano-Furukawa, A., Nishio-Hamane, D., Masly, A., Imaoka, T., and Nakashima, K. (2020) Multi-methodical study of the Ti, Fe^{2+} and Fe^{3+} distribution in chevkinite-subgroup minerals: X-ray diffraction, neutron diffraction, ^{57}Fe Mössbauer spectroscopy and electron-microprobe analyses. Physics and Chemistry of Minerals, 47, 29.

Nelder, J.A., and Mead, R. (1965) A simplex method for function minimization. Computer Journal, 7, 308-313.

Parodi, G.C., Della Ventura, G., Mottana, A., and Raudsepp, M. (1994) Zr-rich non metamict perrierite-(Ce) from holocrystalline ejecta in the Sabatini volcanic complex (Latium, Italy). Mineralogical Magazine, 58, 607-613.

Pen, C.C., and Pan, C.L. (1964) The crystal structure of chevkinite. Scientia Sinica, XIII, 1539-1545 (in Russian).

Platt, R.G., Wall, F., Williams, C.T., and Woolley, A.R. (1987) Zirconolite, chevkinite and other rare earth minerals from nepheline syenites and peralkaline granites and syenites of the Chilwa Alkaline Province, Malawi. Mineralogical Magazine, 51, 253-263.

Popov, V.A., Pautov, L.A., Sokolova, E., Hawthorne, F.C., McCammon, C., and Bazhenova, L.F. (2001) Polyakovite-(Ce), $(REE,Ca)_4(Mg,Fe^{2+})(Cr^{3+},Fe^{3+})_2(Ti,Nb)_2Si_4O_{22}$, a new metamict mineral species from the Ilmen Mountains, Southern Urals, Russia: Mineral description and crystal chemistry. Canadian Mineralogist, 39, 1095-1104.

Ralph, R.L., and Finger, L.W. (1982) A computer program for refinement of crystal orientation matrix and lattice constants from diffractometer data with lattice symmetry constraints. Journal of Applied Crystallography, 15, 537-539.

Rancourt, D.G., McDonald, A.M., Lalonde, A.E., and Ping, J.Y. (1993) Mössbauer absorber thicknesses for accurate site populations in Fe-bearing minerals. American Mineralogist, 78, 1-7.

Ridolfi, F. (2004) REE- and HFSE-minerals in peralkaline syenites: Crystal-chemistry and petrogenetic significance. Plinius, 30, 202-206.

Ridolfi, F., Renzulli, A., Santi, P., and Upton, B.G.J. (2003) Evolutionary stages of crystallization of weakly peralkaline syenites: evidence from ejecta in the plinian deposits of Agua de Pau volcano (São Miguel, Azores Islands). Mineralogical Magazine, 67, 749-767.

Ridolfi, F., Renzulli, A., Macdonald, R., and Upton, B.G.J. (2006) Peralkaline syenite autoliths from Kilombe volcano, Kenya Rift Valley: Evidence for subvolcanic interaction with carbonatitic fluids. Lithos, 91, 373–392.

Robinson, K., Gibbs, G.V., and Ribbe, P.H. (1971) Quadratic elongation: a quantitative measure of distortion in coordination polyhedra. Science, 172, no.3983, 567-570.

Salinas-Sanchez, A., Garcia-Munoz, J.L., Rodriguez-Carvajal, J., Saez-Puche, R., and Martinez, J.L. (1992) Structural characterization of R_2BaCuO_5 (R=Y, Lu, Yb, Tm, Er, Ho, Dy, Gd, Eu and Sm) oxides by X-ray and neutron diffraction. Journal of Solid State Chemistry, 100, 201-211.

Schaltegger, U., Zeilinger, G., Frank, M., and Burg, J. (2002) Multiple mantle sources during island arc magmatism; U-Pb and Hf isotopic evidence from the Kohistan arc complex, Pakistan. Terra Nova, 14(6), 461-468.

Searle, M.P., Khan, M.A., Fraser, J.E., Gough, S.J., and Qasim, J.M. (1999) The tectonic evolution of the Kohistan-Karakoram collision belt along the Karakoram Highway transect, North Pakistan. Tectonics, 18(6), 929-949.

Segalstad, T.V., and Larsen, A.O. (1978) Chevkinite and perrierite from the Oslo region, Norway. American Mineralogist, 63, 499-505.

Shannon, R.D. (1976) Revised effective radii and systematic studies of interatomic distances in halides and chalcogenides. Acta Crystallographica, A32, 751-767.

Sheldrick, G.M. (1997) SHELXL-97, a program for crystal structure refinement. University of Göttingen, Germany.

Shellnutt, J.G., and Iizuka, Y. (2013) Chevkinite-group minerals from the mantle-derived metaluminous Woshui syenite of the Emeishan large igneous province. European Journal of Mineralogy, 25, 671-682.

Sokolova, E., and Hawthorne, F.C. (2004) The crystal chemistry of silicate minerals with chains of (TiO_6) octahedra. Canadian Mineralogist, 42, 807-824.

Sokolova, E., Hawthorne, F.C., Della Ventura, G., and Kartashov, P.M. (2004) Chevkinite-(Ce): Crystal structure and the effect of moderate radiation-induced damage on site-occupancy refinement. Canadian Mineralogist, 42,1129-1141.

Song, R., Ding, K., and Li, Z. (1999) Site occupancies of iron in saimaite and chevkinite. Chinese Science Bulletin, 44, 2274-2276.

Stachowicz, M., Bagiński, B., Welch, M.D., Kartashov, P.M., Macdonald, R., Balcerzak, J., Tyczkowski, J., and Woźniak, K. (2019a) Cation ordering, valence states, and symmetry breaking in the crystal-chemically complex mineral chevkinite-(Ce): X-ray diffraction and photoelectron spectroscopy studies and mechanisms of Nb enrichment. American Mineralogist, 104, 595-602.

Stachowicz, M., Welch, M.D., Bagiński, B., Kartashov, P.M., Macdonald, R., and Woźniak, K. (2019b) Cation ordering, valence states, and symmetry breaking in the crystal-chemically complex mineral chevkinite-(Ce): Recrystallization, transformation, and metamict states in chevkinite. American Mineralogist, 104, 1481-1486.

Tokonami, M. (1965) Atomic scattering factor for O^{2-}. Acta Crystallographica, 19, 486.

Troll, V.R., Sachs, P.M., Schmincke, H.-U., and Sumita, M. (2003) The REE-Ti mineral chevkinite in comenditic magmas from Gran Canaria, Spain: A SYXRF-probe study. Contribution to Mineralogy and Petrology, 145, 730-741.

Ungaretti, L., Lombardo, B., Domeneghetti, C., and Rossi, G. (1983) Crystal-chemical evolution of amphiboles from eclogitised rocks of the Sesia-Lanzo zone, Italian Western Alps. Bulletin de Minéralogie, 106, 645-672.

Vasquez, J.A., Velasco, N.O., Schmitt, A.K., Bleick, H.A., and Stelten, M.E. (2014) ^{238}U-^{230}Th dating of chevkinite in high-silica rhyolites from La Primavera and Yellowstone calderas. Chemical Geology, 390, 109-118.

Vlach, S.R.F., and Gualda, G.A.R. (2007) Allanites and chevkinites in A-type granites and syenites of the Graciosa Province, Southern Brazil. Lithos, 97, 98-121.

Walker, G.P.L., and Croasdale, R. (1970) Two plinian-type eruptions in the Azores. Journal of the Geological Society of London, 127, 17-55.

Widom, E., Schmincke, H.-U., and Gill, J.B. (1992) Processes and timescales in the evolution of a chemical zoned trachyte: Fogo-A, São Miguel, Azores. Contribution to Mineralogy and Petrology, 111, 311-328.

Widom, E., Gill, J.B., and Schmincke, H.-U. (1993) Syenite nodules as a long-term record of magmatic activity in Agua de Pau Volcano, São Miguel, Azores. Journal of Petrology, 34, 929-953.

Wilson, A.J.C. (1992) International Tables for Crystallography, Volume C, 883 p. Kluwer Academic Publishers, Dordrecht, the Netherlands.

X-SHAPE STOE, Version1.06 (1999) Crystal optimisation for numerical absorption correction. STOE and CIE Gmbh, Darmstadt.

Xu, J., Yang, G., Li, G., Wu, Z., and Shen, G. (2008) Dingdaohengite-(Ce) from the Bayan-Obo REE-Nb-Fe mine, China: Both a true polymorph of perrierite-(Ce) and a titanic analog at the C1 site of chevkinite subgroup. American Mineralogist, 93, 740-744.

Yang, Z., Fleck, M., Smith, M., Tao, K., Song, R., and Zhang, P. (2002) The crystal structure of natural Fe-rich chevkinite-(Ce). European Journal of Mineralogy, 14, 969-975.

Yang, Z., Li, H., Liu, M., and Pertlik, F. (2007) Crystal chemistry of iron in non-metamict Chevkinite-(Ce): Valence state and site occupation proportions. Journal of Rare Earths, 25, 238-242.

Yang, Z., Pertlik, F., and Fleck, M. (2008) Hydroxyl groups in nonmetamict chevkinite-(Ce): A crystal chemical discussion. Journal of Rare Earths, 26, 4, 609-613.

Zeitler, K. (1985) Cooling history of the NW Himalaya, Pakistan. Tectonics, 4(1), 127-151.

Figure captions

Figure 1. (010) projection of chevkinite-(Ce) structure (*C2/m*) showing the rutile layer and the silicate layer stacked along *c**. The rutile layer is composed of alternatively attached edge-sharing C chains (octahedral C1 sites) and edge-sharing D chains (octahedral C2A-C2B sites) running parallel to the *b*-axis. The silicate layer is composed of the A1 and A2 polyhedra, the Si_2O_7 disilicate group, and the B octahedron.

Figure 2. Backscattered electron (BSE) images of chevkinite crystals of three syenite samples of Agua de Pau (LdF5, LdF4, LdF1). **A: (**LdF5) Subhedral chevkinite-(Ce) crystal (Chv) interstitial between alkali feldspar (Afs), amphibole (Amp), and ilmenite (Ilm), in contact with apatite (Ap) and enclosing titanomagnetite (Tmag). One small crystal of Chv is also enclosed in the amphibole. **B: (**LdF4) Subhedral Chv crystal interstitial between Afs and two Amp crystals, and enclosing britholite-apatite solid-solution (Brt-Ap). At the left margin of chevkinite, two idiomorphic crystals of zircon (Zrn) are present. **C: (**LdF1) Subhedral crystal of Chv interstitial between Afs, Amp, and orthopyroxene (Opx) and enclosing Tmag, Ap, and Zrn. **D: (**LdF4) Subhedral Chv crystal interstitial between Afs and associated with Ilm and extensively altered Ap. **E: (**LdF1) Anhedral Chv with quite irregular margins in contact with Afs and enclosing britholite-(Ce) (Brt) and aegirine (Aeg), both showing marginal resorption. Chv and Brt are both characterized by complex patchy zoning, the variations in brightness being mainly due to differences in Ca and REE contents. **F**: (LdF1) Subhedral Chv crystal interstitial between Afs. At the left and bottom margins, a chaotic intergrowth of Aeg and irregularly rimmed bright phases, monazite (Mnz) and heavily resorbed Brt are apparent; a subhedral crystal of pyrochlore (Pcl) is also present.

Figure 3. Representative SEM chemical maps of Ca, La, Ce, and Nb for the Chv crystals of Fig. 2 E (**A** and **B**), Fig. 2 F (**C** and **D**) and Fig. 2 D (**E** and **F**). In (**A**) and (**B**), Brt shows incipient alteration inducing REE remobilization. In (**C**) and (**D**), patchy zoning is evident by different degrees of brightness (Fig. 2 F) and differences in Ca and REE contents. In (**E**) and (**F**), weak curvilinear boundaries delimitate areas enriched in Ca and Nb from REE- and Fe-rich zones.

Figure 4. CaO vs. FeO* discriminator diagram of Macdonald and Belkin (2002) (modified) separating chevkinite and perrierite compositions. The area enclosed by a continuous line represents the most populated chevkinite field from the literature. All AZ and PAK analyses are shown (Supplementary Table S1).

Figure 5. (a) (Ca+Ti+Zr) vs. (REE+Fe^{2+}+Nb) relationship in AZ chevkinites (all analyses; continuous line is the linear fit $y = -1.068x + 8.511$ with $R^2 = 0.94$). Notably, in patchily zoned crystals 9 and 74, the charge balance relationship is comparable with that of the other studied crystals. **(b)** Zr vs. Nb (apfu) plot in AZ chevkinites. Symbols as in Fig. 5a.

Figure 6. Example of SAED pattern along the [010] axis from a micro-grain of Azores sample (AZ33). The absence of streaked spots indicates the absence of structural defects in the layer alternation.

Figure 7. Detail of the linkage between the A2 and Si2 polyhedra along a plane parallel to the *b* axis. The two polyhedra share the O3-O3 edge. Arrows indicate the shift in the relative positions of A2 and O3 atoms in crystals 75, 74, and 9 in which the A2-O3 bond lengths become shorter than A2-O1 (see text). To simplify the drawing, the A2-O2 and A2-O8 bond lengths are omitted.

Figure 8. 11K Mössbauer spectrum of Pakistan chevkinite. Black dots represent the experimental data, black line the calculated spectrum; red line stands for ferric Db1 site, blue and green lines represent ferrous Db2 and Db3 sites, respectively.

Figure 9. <B-O> mean bond length vs. cell volume plot in natural chevkinite-(Ce) samples, partly metamict and non-metamict with $C2/m$ and $P2_1/a$ structure refinements. Vertical dash lines drawn to approximately separate the fields.

APPENDIX A

1) $\sigma_{N'_{Fe^{3+}}}$ error of $N'_{Fe^{3+}}$, the atomic fraction of Fe^{3+}, calculated for N_O oxygens and N_{CT} cations:

$$\sigma_{N'_{Fe^{3+}}} = \frac{2N_O - N'_{Fe^{3+}}}{N_{CT}} \sqrt{\sum \sigma^2{}_{N'_i} + \left(1 + \frac{N'_{Fe^{3+}}}{N'_{Fe^{2+}}}\right)^2 \sigma^2_{N'_{Fe^{2+}}}} \, ,$$

where $\sigma_{N'_i}$ is the standard deviation of the atomic fraction i different from $N'_{Fe^{2+}}$.

1bis) σ' mean error of the atomic fraction of Fe^{3+}:

$\sigma' = \frac{\sigma_{N'_{Fe^{3+}}}}{\sqrt{n}}$ where n is the number of point analyses.

2) $\sigma_{e^-_{ref}}$ error of the total electrons from site occupancy refinement in the A, B, C, and D sites for chevkinite formula $A_4BC_2D_2O_8(Si_2O_7)_2$:

$$\sigma_{e^-_{ref}} = \sqrt{\left(2\sigma_{e^-_{refA1}}\right)^2 + \left(2\sigma_{e^-_{refA2}}\right)^2 + \left(\sigma_{e^-_{refB}}\right)^2 + \left(2\sigma_{e^-_{refC1}}\right)^2 + \left(\sigma_{e^-_{refC2A}}\right)^2 + \left(\sigma_{e^-_{refC2B}}\right)^2} \, .$$

3) $\sigma_{e^-_{chem}}$ error of the total electrons from chemical analysis in the A, B, C, and D sites for chevkinite formula $A_4BC_2D_2O_8(Si_2O_7)_2$:

$$\sigma_{e^-_{chem}} = \sqrt{\sum (\sigma_i Z_i)^2} \, ,$$

where σ_i and Z_i are the estimated standard deviation and the atomic number of each analyzed element, respectively.

4) $\overline{x}_w$ weighted average of the bond distances:

$$\overline{x}_w = \frac{\sum \frac{x_i}{\sigma_i}}{\sum \frac{1}{\sigma_i}} \, ,$$

where x_i is each individual bond length, and σ_i is its estimated standard deviation.

4bis) $\sigma_{\overline{x}_w}$ error of the weighted average of the bond distances:

$$\sigma_{\overline{x}_w} = \sqrt{\frac{\sum \frac{1}{\sigma_i}(x_i - \overline{x}_w)^2}{\sum \frac{1}{\sigma_i}}} \, .$$

APPENDIX B

Crystallographic direction of the edge	frequency
[100]	1
[101]	1
[10-1]	1
[01-1]	1
[012]	1
[1-1-1]	1
[1-1-3]	1
[203]	1
[213]	1
[3-1-3]	1
[313]	1
[315]	1
[-3-11]	1
[40-3]	1
[512]	1
[5-11]	1
[531]	1

Table 1B. Crystallographic direction of the different edge (as deduced from the corresponding SAED pattern) with its frequency for different microcrystals.

Figure 1

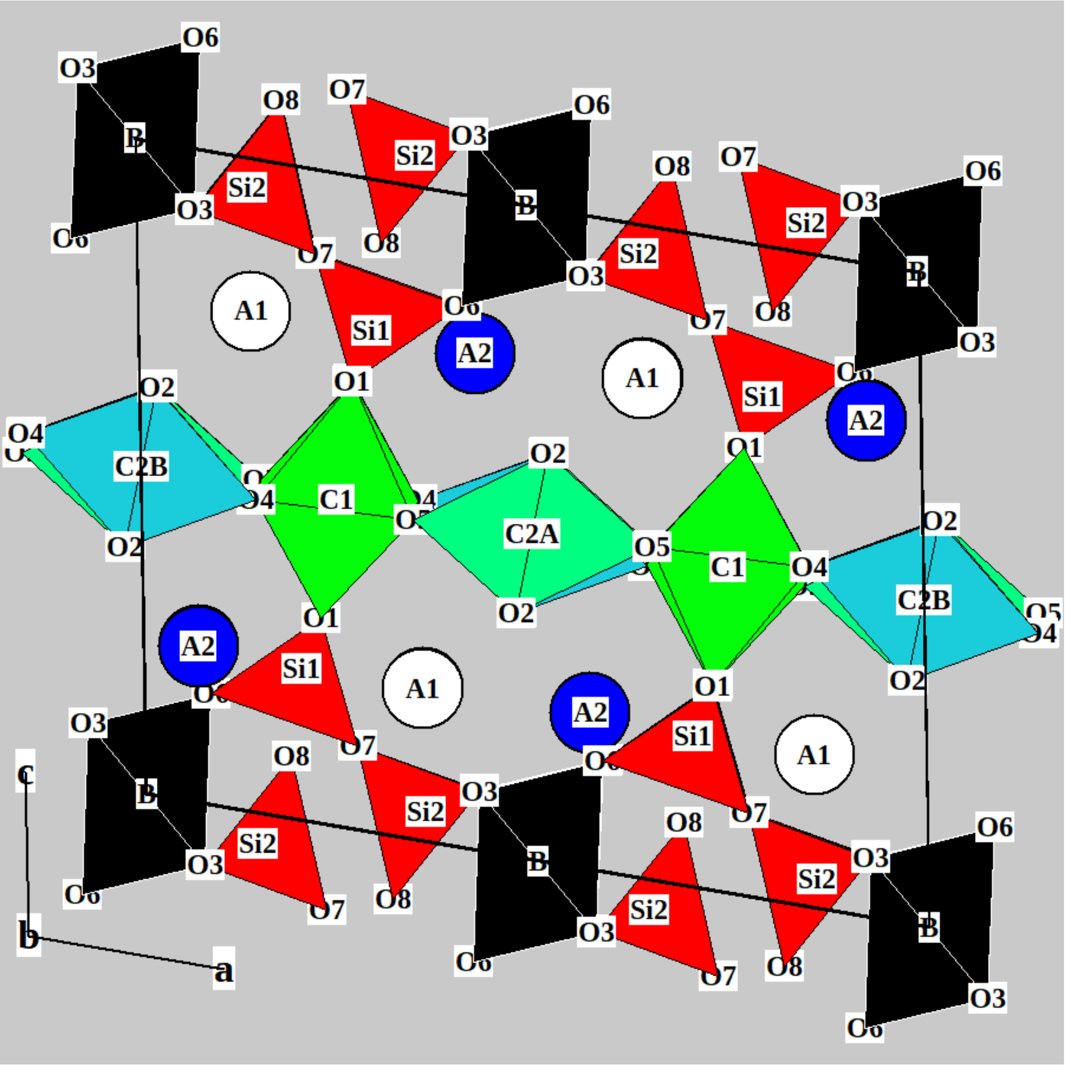

Figure 2

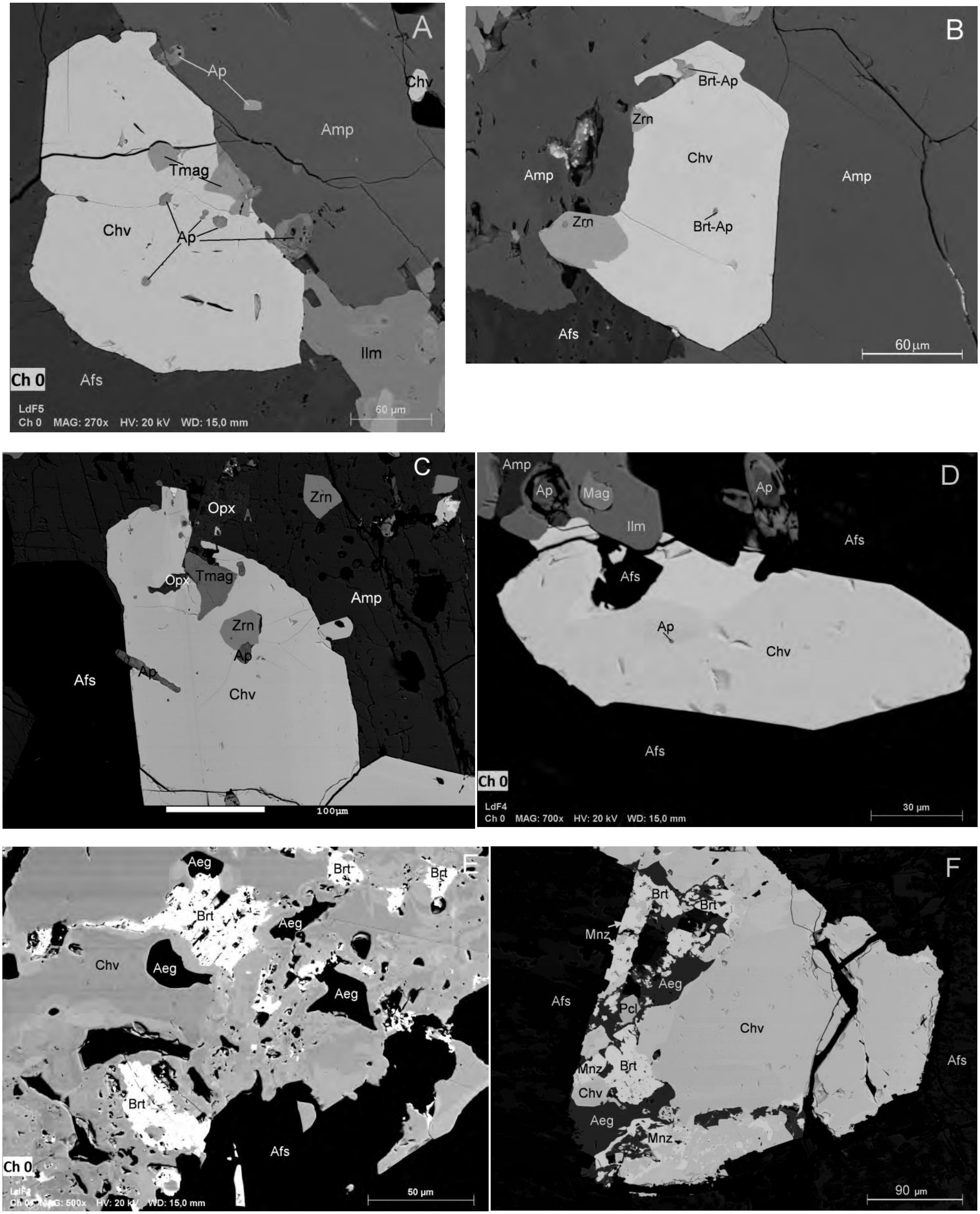
A
Ap
Chv
Amp
Tmag
Chv
Ap
Ilm
Ch 0
Afs
LdF5
Ch 0 MAG: 270x HV: 20 kV WD: 15,0 mm
60 µm
B
Brt-Ap
Zrn
Chv
Amp
Amp
Zrn
Brt-Ap
Afs
60 µm
C
Zrn
Opx
Opx
Tmag
Amp
Zrn
Ap
Ap
Afs
Chv
100µm
D
Amp
Ap
Mag
Ap
Ilm
Afs
Afs
Ap
Chv
Afs
Ch 0
LdF4
Ch 0 MAG: 700x HV: 20 kV WD: 15,0 mm
30 µm
E
Aeg
Brt
Brt
Brt
Aeg
Chv
Aeg
Aeg
Brt
Afs
Ch 0
MAG: 500x HV: 20 kV WD: 15,0 mm
50 µm
F
Brt
Brt
Mnz
Aeg
Afs
Pcl
Chv
Mnz
Brt
Chv
Aeg
Mnz
Afs
90 µm

Figure 3

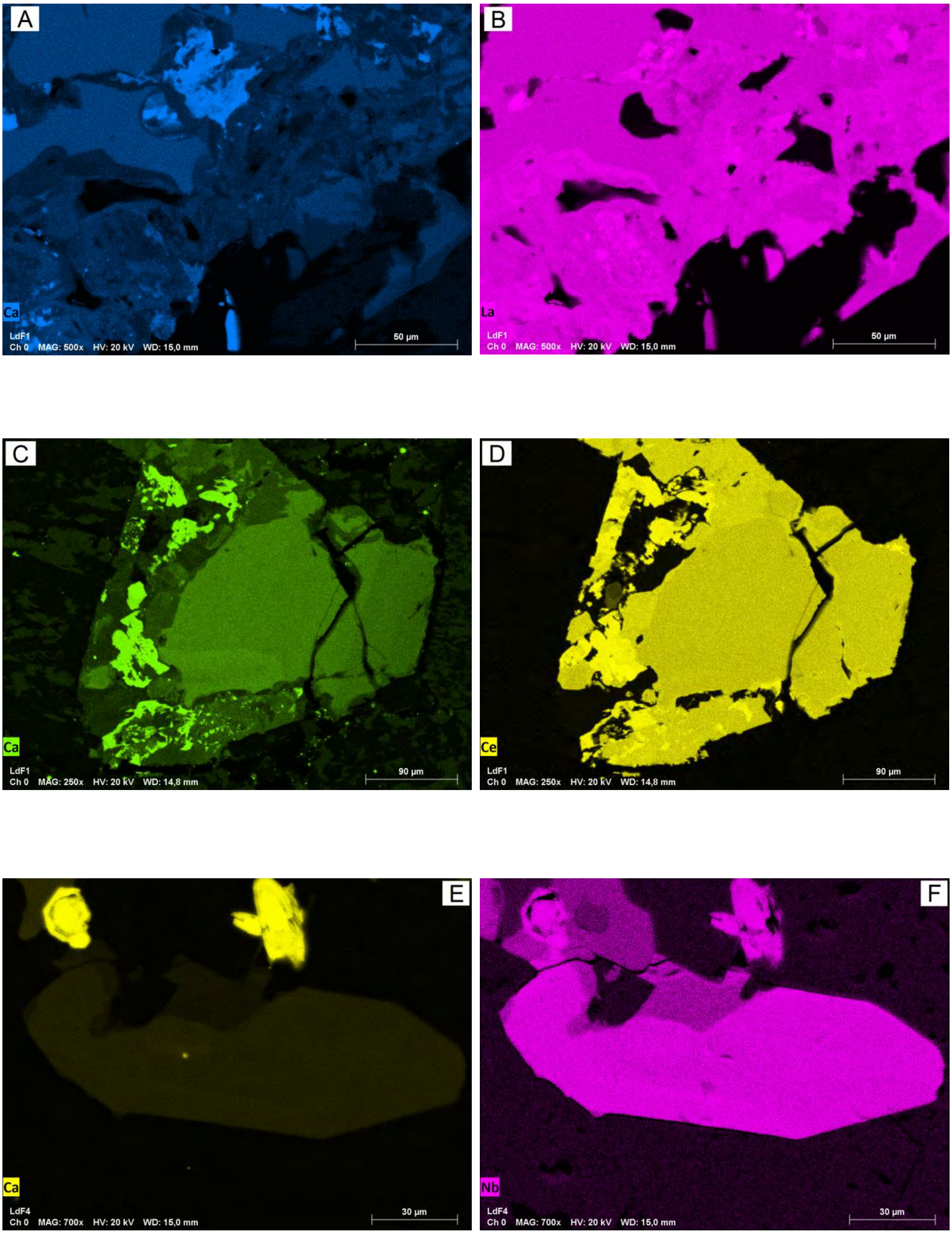
A
Ca
LdF1
Ch 0 MAG: 500x HV: 20 kV WD: 15,0 mm
50 µm
B
La
LdF1
Ch 0 MAG: 500x HV: 20 kV WD: 15,0 mm
50 µm
C
Ca
LdF1
Ch 0 MAG: 250x HV: 20 kV WD: 14,8 mm
90 µm
D
Ce
LdF1
Ch 0 MAG: 250x HV: 20 kV WD: 14,8 mm
90 µm
E
Ca
LdF4
Ch 0 MAG: 700x HV: 20 kV WD: 15,0 mm
30 µm
F
Nb
LdF4
Ch 0 MAG: 700x HV: 20 kV WD: 15,0 mm
30 µm

Figure 4

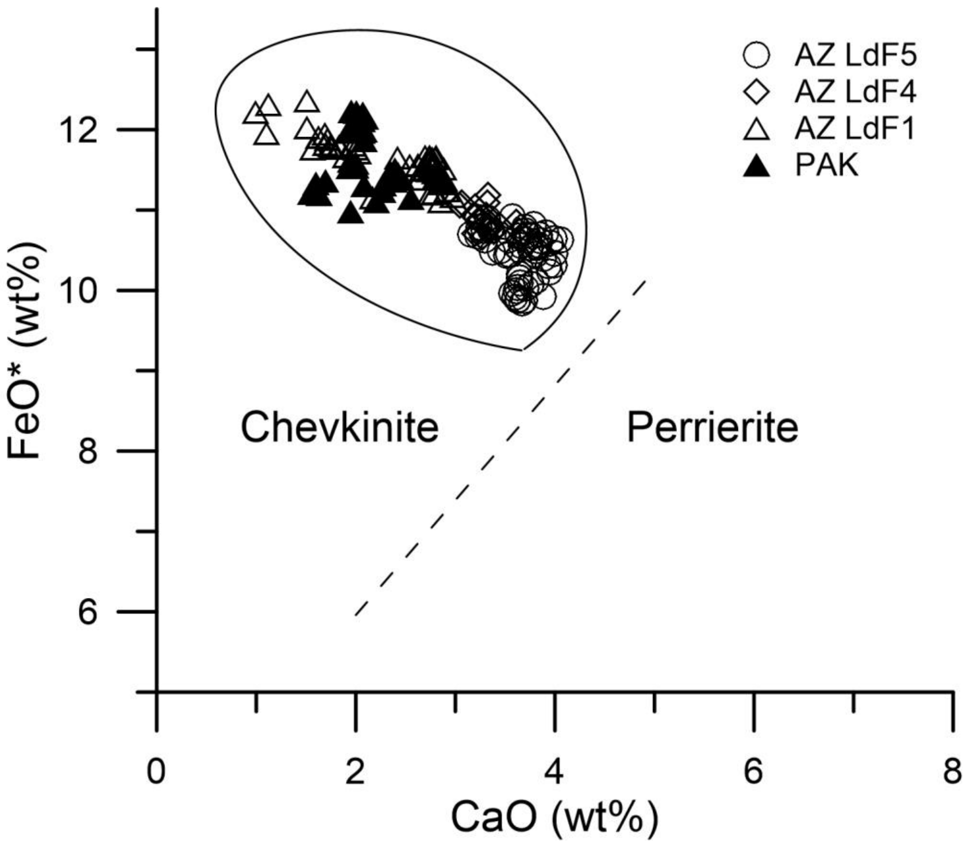
○ AZ LdF5
◇ AZ LdF4
△ AZ LdF1
▲ PAK
Chevkinite
Perrierite
FeO* (wt%)
12
10
8
6
0
2
4
6
8
CaO (wt%)

Figure 5a

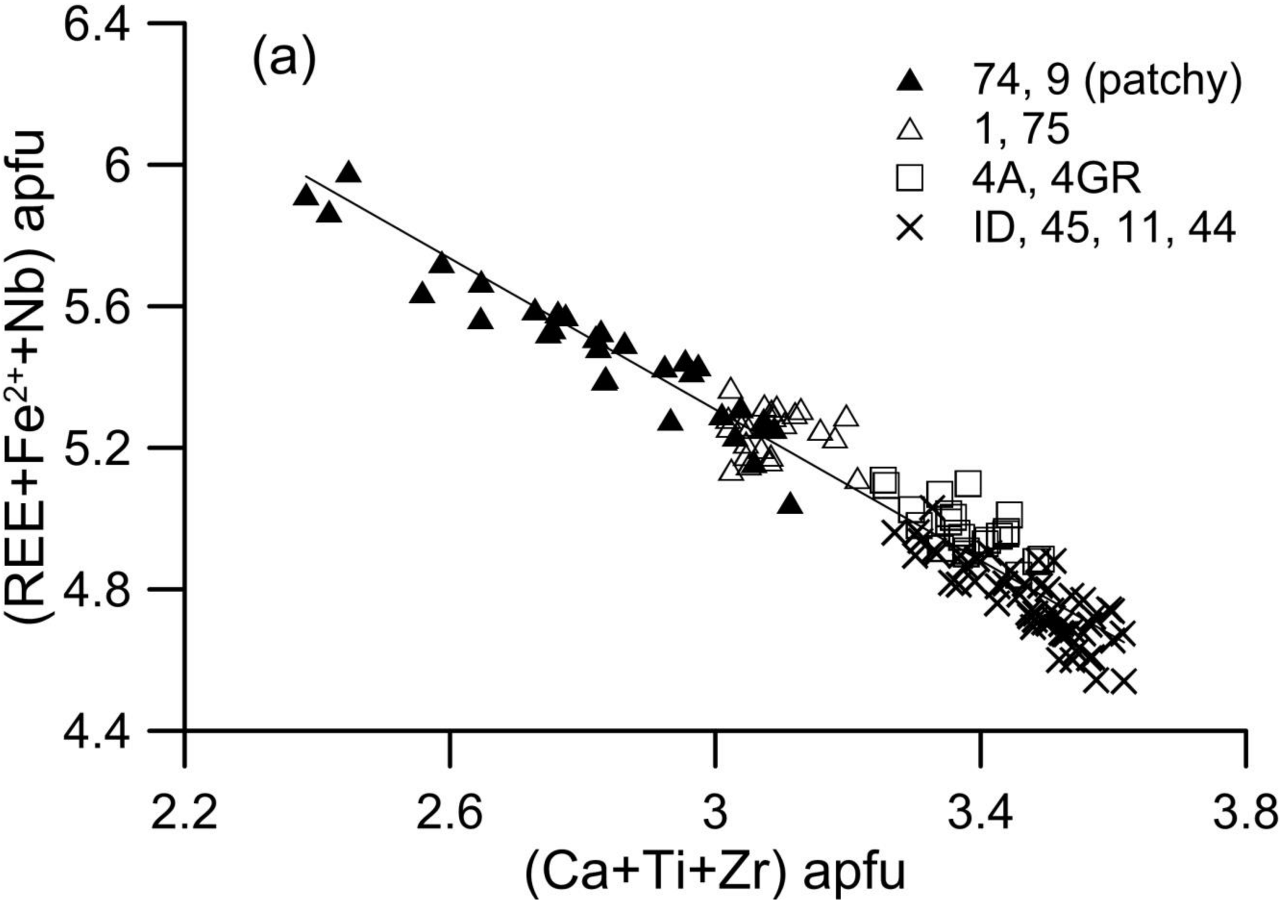
(a)
▲ 74, 9 (patchy)
△ 1, 75
□ 4A, 4GR
× ID, 45, 11, 44
(REE+Fe^{2+}+Nb) apfu
6.4
6
5.6
5.2
4.8
4.4
2.2
2.6
3
3.4
3.8
(Ca+Ti+Zr) apfu

Figure 5b

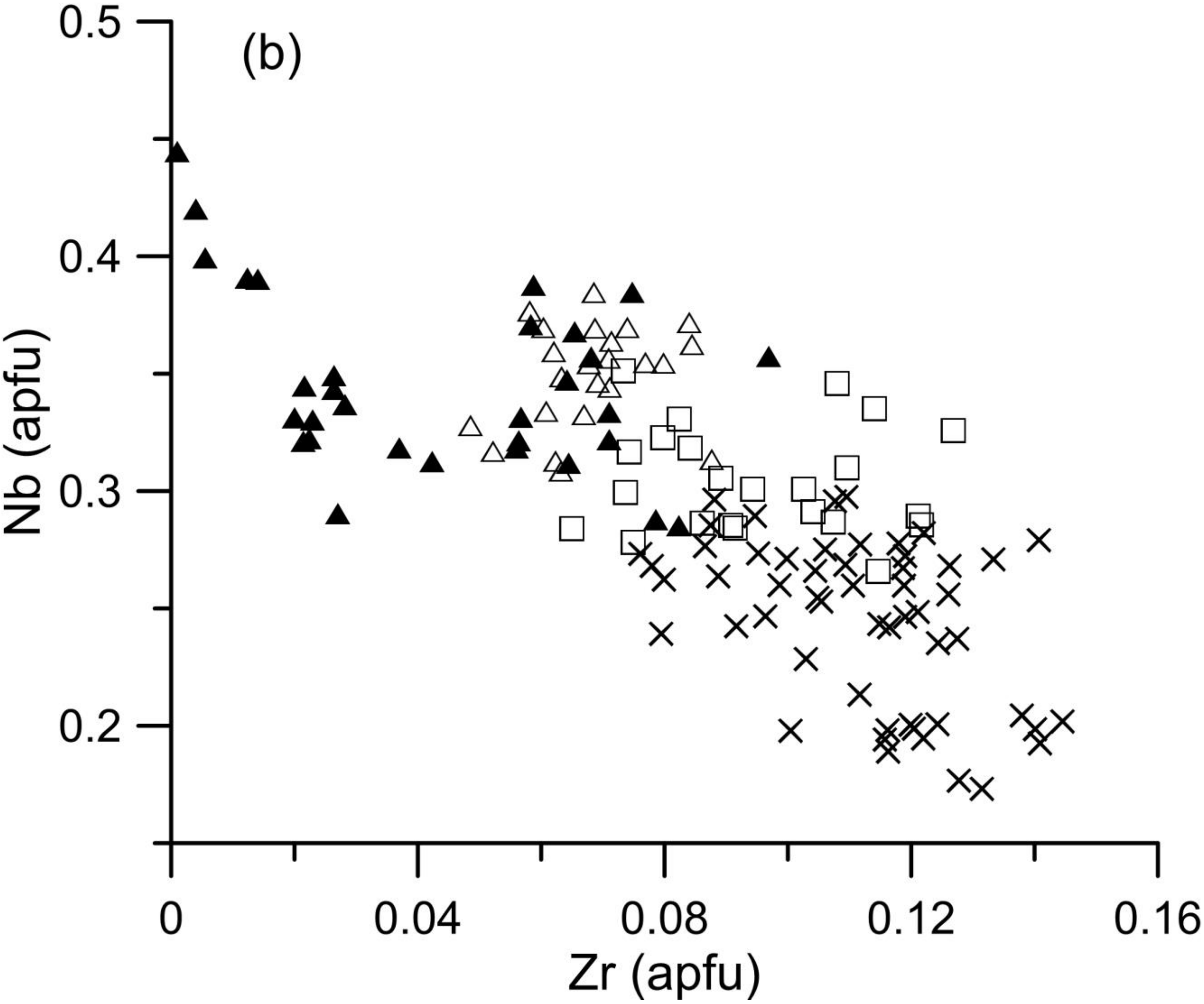

Figure 6

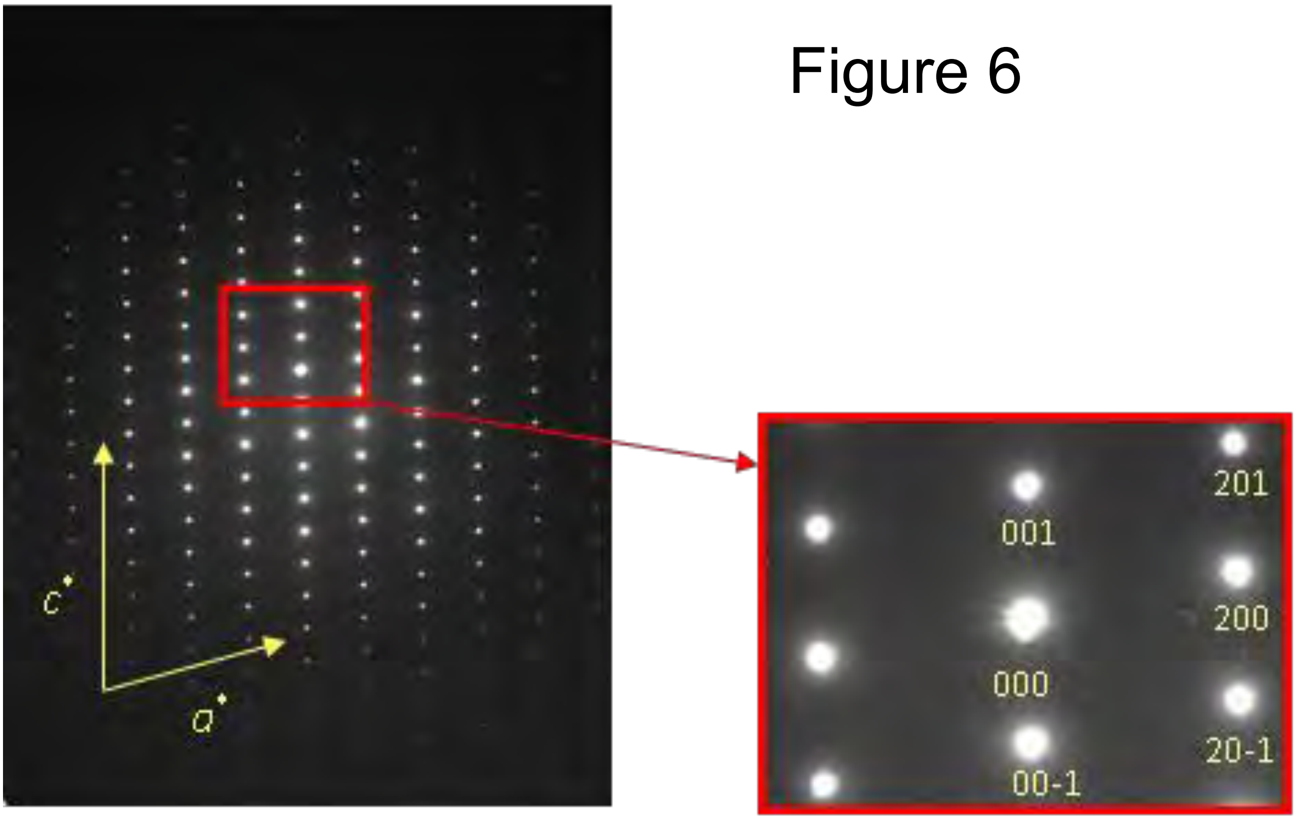

Figure 7

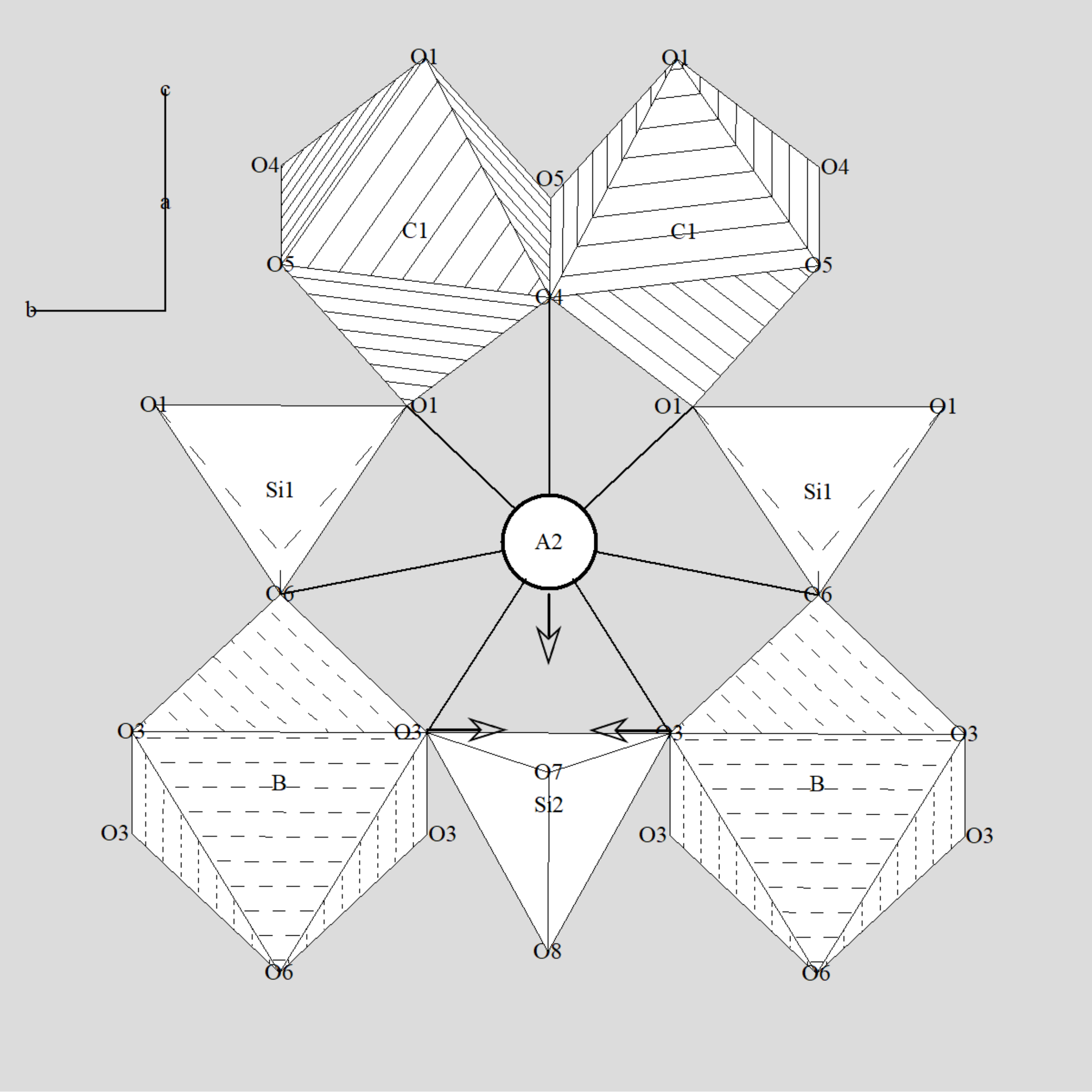
c
a
b
O1
O1
O4
O5
O4
C1
C1
O5
O5
O4
O1
O1
O1
O1
Si1
Si1
A2
O6
O6
O3
O3
O3
O3
B
B
O7
Si2
O3
O3
O3
O3
O8
O6
O6

Figure 8

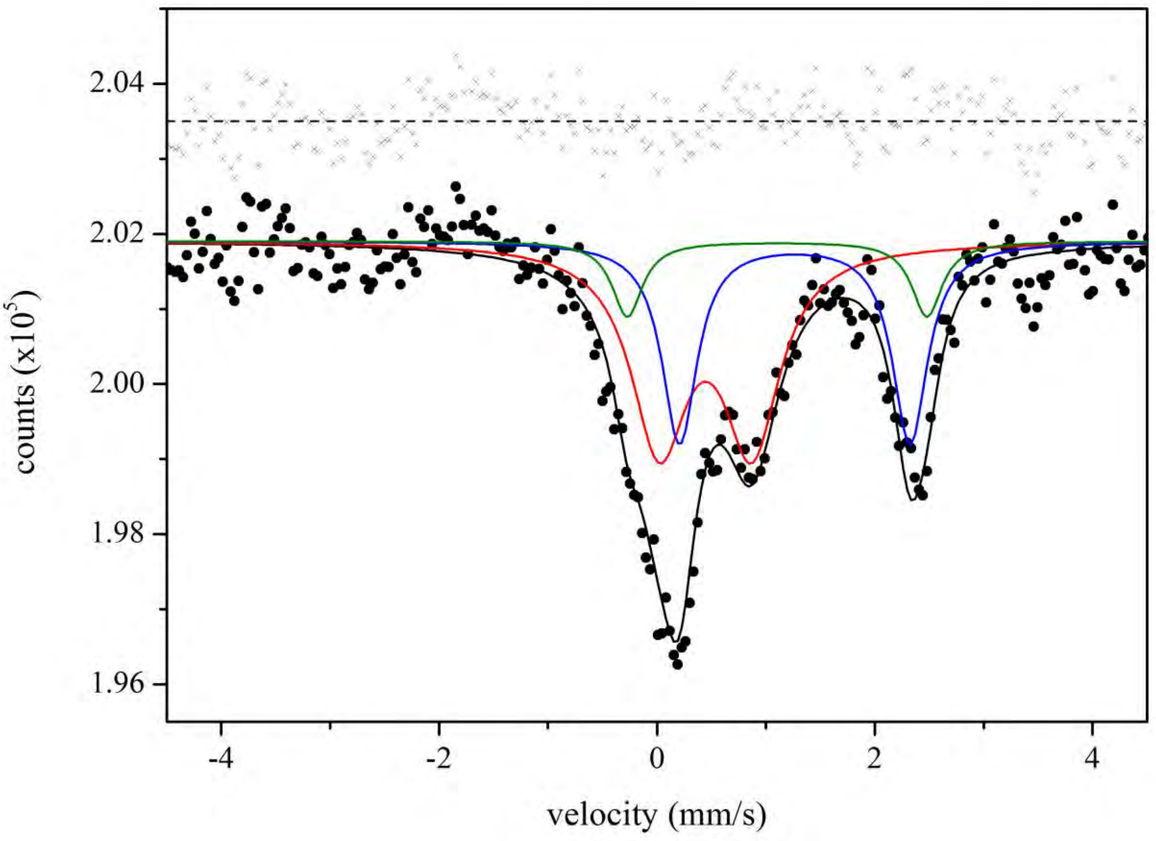

Figure 9

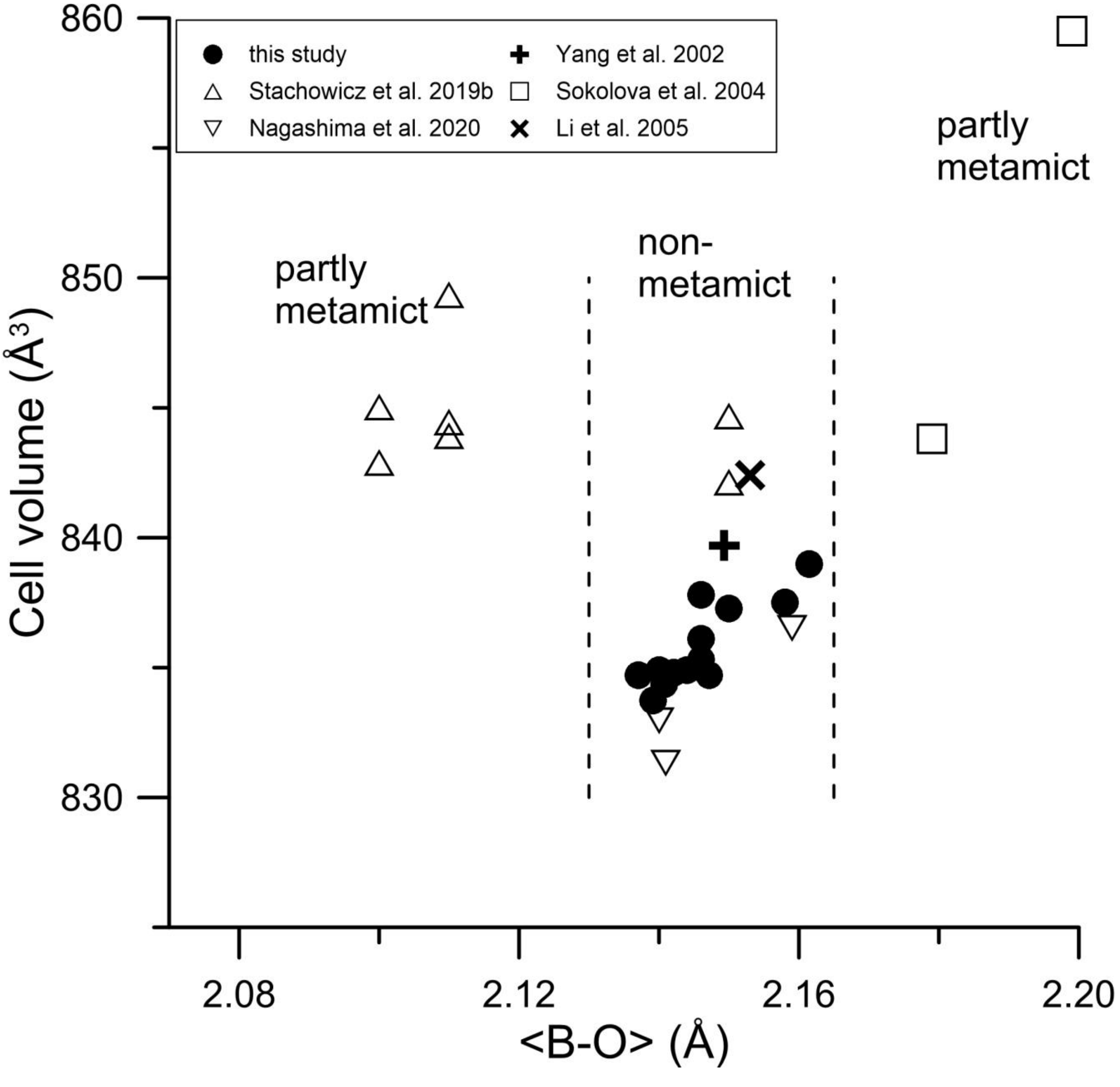
860
850
840
830
Cell volume (Å^3)
2.08
2.12
2.16
2.20
<B-O> (Å)
● this study
△ Stachowicz et al. 2019b
▽ Nagashima et al. 2020
✚ Yang et al. 2002
□ Sokolova et al. 2004
✖ Li et al. 2005
partly metamict
non-metamict
partly metamict

Table 1. Average microprobe compositions (wt%) of Azores (AZ) and Pakistan (PAK) chevkinites. Number in parentheses refers to standard deviation.

host rock	**AZ LdF5**				**AZ LdF4**		**AZ LdF1**				**PAK**		
sample	**ID**	**45**	**11**	**44**	**4A**	**4GR**	**1**	**75**	**74**	**9**	**6**	**7**	**4**
no. pts.	15	11	12	16	11	12	8	15	19	12	9	10	10
MgO	0.39 (5)	0.20 (6)	0.15 (4)	0.19 (5)	0.15 (4)	0.13 (5)	0.03 (5)	0.03 (4)	b.d.l.	b.d.l.	0.31 (6)	0.30 (5)	0.37 (4)
Al_2O_3	0.31 (2)	0.18 (5)	0.17 (3)	0.19 (5)	0.16 (3)	0.16 (3)	0.09 (4)	0.05 (3)	0.03 (3)	0.03 (4)	0.18 (3)	0.09 (5)	0.20 (4)
SiO_2	20.01 (10)	19.74 (12)	19.86 (15)	19.98 (22)	19.46 (14)	19.58 (12)	19.31 (6)	19.53 (9)	19.46 (14)	19.27 (32)	19.50 (15)	19.30 (13)	19.29 (10)
CaO	3.67 (8)	3.33 (13)	3.69 (14)	3.88 (12)	3.26 (12)	3.44 (18)	2.84 (8)	2.76 (6)	2.17 (42)	1.84 (70)	2.29 (19)	1.95 (33)	2.04 (6)
TiO_2	17.22 (14)	16.39 (16)	16.65 (19)	16.95 (19)	16.53 (19)	16.58 (14)	15.71 (20)	15.28 (17)	15.05 (19)	14.43 (72)	17.17 (17)	17.22 (22)	16.51 (10)
MnO	0.34 (3)	0.45 (5)	0.45 (4)	0.41 (4)	0.47 (5)	0.45 (5)	0.52 (6)	0.50 (05)	0.58 (9)	0.62 (11)	0.56 (7)	0.71 (6)	0.35 (4)
FeO*	10.00 (11)	10.66 (14)	10.72 (12)	10.49 (13)	10.91 (15)	10.77 (17)	11.31 (15)	11.56 (10)	11.64 (30)	11.83 (36)	11.44 (8)	11.25 (17)	12.08 (13)
SrO	b.d.l.	b.d.l.	b.d.l.	b.d.l.	b.d.l.	b.d.l.	b.d.l.	b.d.l.	b.d.l.	b.d.l.	0.24 (17)	0.27 (11)	0.33 (10)
Y_2O_3	0.29 (10)	0.22 (13)	0.21 (12)	0.27 (11)	0.27 (7)	0.23 (10)	0.22 (12)	0.18 (12)	0.18 (10)	0.17 (10)	b.d.l.	0.10 (11)	b.d.l.
ZrO_2	1.27 (13)	0.91 (12)	1.15 (15)	1.14 (13)	0.88 (15)	1.03 (19)	0.72 (10)	0.65 (9)	0.50 (22)	0.33 (30)	0.20 (7)	0.12 (11)	0.13 (6)
Nb_2O_5	2.14 (11)	2.91 (19)	2.96 (20)	2.81 (16)	3.22 (21)	3.35 (28)	3.87 (24)	3.67 (22)	3.52 (28)	3.89 (44)	0.42 (7)	0.47 (12)	0.40 (8)
La_2O_3	13.28 (40)	13.25 (34)	13.17 (47)	12.83 (32)	13.19 (25)	13.16 (41)	13.80 (15)	13.97 (37)	13.51 (52)	14.24 (43)	10.70 (37)	10.65 (28)	10.20 (22)
Ce_2O_3	22.38 (42)	22.59 (37)	22.57 (41)	22.43 (43)	22.12 (60)	22.05 (33)	22.59 (33)	23.35 (35)	24.16 (66)	24.39 (87)	23.43 (42)	24.22 (41)	23.94 (57)
Pr_2O_3	1.77 (26)	1.90 (22)	1.78 (21)	1.85 (23)	1.80 (16)	1.68 (18)	1.89 (21)	1.76 (20)	1.91 (20)	1.98 (25)	2.22 (31)	2.37 (24)	2.41 (17)
Nd_2O_3	5.34 (19)	5.49 (22)	5.27 (21)	5.27 (29)	5.53 (26)	5.44 (21)	5.27 (21)	5.25 (24)	5.82 (56)	5.76 (56)	7.87 (21)	8.32 (43)	8.06 (38)
Sm_2O_3	0.40 (15)	0.40 (10)	0.42 (17)	0.46 (10)	0.50 (13)	0.48 (13)	0.47 (13)	0.47 (15)	0.46 (16)	0.51 (13)	0.57 (11)	0.63 (10)	0.65 (17)
Gd_2O_3	0.24 (12)	0.30 (12)	0.18 (12)	0.27 (9)	0.24 (11)	0.22 (13)	0.19 (11)	0.20 (10)	0.27 (11)	0.26 (16)	0.19 (10)	0.21 (13)	0.25 (12)
ThO_2	1.00 (18)	0.98 (12)	0.75 (15)	0.78 (8)	1.07 (12)	0.89 (12)	0.89 (16)	0.87 (7)	0.68 (12)	0.52 (18)	1.55 (29)	0.97 (20)	1.76 (14)
Total	100.04	99.90	100.14	100.19	99.76	99.62	99.71	100.08	99.92	100.08	98.87	99.14	98.95
FeO	7.39	7.95	7.85	7.71	8.32	8.47	8.98	8.66	9.06	9.09	6.67	6.70	6.29
Fe_2O_3	2.89	3.00	3.19	3.09	2.88	2.56	2.59	3.22	2.87	3.05	5.30	5.05	6.43
Total	100.33	100.21	100.46	100.50	100.05	99.88	99.97	100.41	100.20	100.39	99.40	99.65	99.60

no. pts.: number of spot analyses. FeO*: all Fe as FeO; all FeO was divided into Fe^{2+} and Fe^{3+} based on the charge balance of the empirical formula calculated for 13 cations and 22 O.

b.d.l.: below limit of detection.

Table 2. Average structural formulae of Azores (AZ) and Pakistan (PAK) chevkinites on the basis of 22 oxygens and 13 cations. Number in parentheses refers to standard deviation.

host rock	**AZ LdF5**				**AZ LdF4**		**AZ LdF1**				**PAK**		
sample	**ID**	**45**	**11**	**44**	**4A**	**4GR**	**1**	**75**	**74**	**9**	**6**	**7**	**4**
Mg	0.119 (16)	0.062 (17)	0.045 (11)	0.057 (15)	0.047 (11)	0.039 (17)	0.008 (14)	0.009 (14)			0.096 (19)	0.091 (17)	0.116 (13)
Al	0.074 (5)	0.043 (11)	0.042 (7)	0.044 (12)	0.039 (7)	0.038 (7)	0.023 (11)	0.012 (8)	0.008 (8)	0.009 (10)	0.043 (9)	0.022 (13)	0.048 (10)
Si	4.043 (29)	4.035 (26)	4.026 (24)	4.032 (39)	3.988 (22)	4.004 (21)	3.998 (22)	4.037 (18)	4.061 (23)	4.047 (38)	4.039 (29)	4.013 (16)	4.013 (27)
Ca	0.796 (17)	0.730 (26)	0.800 (29)	0.839 (26)	0.715 (29)	0.754 (37)	0.629 (18)	0.611 (14)	0.485 (91)	0.415 (152)	0.507 (40)	0.434 (72)	0.454 (12)
Ti	2.618 (18)	2.520 (26)	2.538 (25)	2.574 (33)	2.548 (34)	2.551 (20)	2.447 (26)	2.376 (25)	2.362 (20)	2.279 (91)	2.675 (24)	2.693 (26)	2.583 (17)
Mn	0.059 (5)	0.078 (9)	0.077 (7)	0.070 (6)	0.082 (8)	0.077 (8)	0.091 (11)	0.088 (9)	0.103 (17)	0.111 (20)	0.099 (11)	0.126 (11)	0.062 (7)
Fe^{2+}	1.250 (46)	1.360 (55)	1.331 (59)	1.301 (50)	1.426 (28)	1.449 (62)	1.555 (41)	1.498 (45)	1.581 (57)	1.596 (120)	1.155 (95)	1.166 (65)	1.095 (52)
Sr											0.029 (21)	0.033 (13)	0.040 (12)
Y	0.031 (11)	0.024 (14)	0.023 (13)	0.029 (12)	0.030 (8)	0.025 (10)	0.024 (14)	0.019 (13)	0.020 (10)	0.019 (11)		0.011 (12)	
Zr	0.125 (12)	0.091 (11)	0.113 (15)	0.112 (13)	0.088 (15)	0.102 (19)	0.073 (11)	0.066 (9)	0.051 (22)	0.034 (30)	0.021 (7)	0.012 (11)	0.013 (6)
Nb	0.196 (10)	0.269 (18)	0.271 (19)	0.256 (14)	0.298 (19)	0.310 (25)	0.362 (22)	0.343 (20)	0.332 (25)	0.369 (45)	0.040 (7)	0.044 (11)	0.038 (7)
La	0.990 (28)	0.999 (25)	0.984 (33)	0.955 (22)	0.997 (15)	0.993 (30)	1.054 (11)	1.065 (25)	1.040 (37)	1.103 (34)	0.818 (27)	0.817 (20)	0.782 (18)
Ce	1.656 (31)	1.691 (24)	1.675 (32)	1.657 (32)	1.659 (38)	1.651 (22)	1.712 (16)	1.767 (26)	1.846 (59)	1.874 (87)	1.776 (35)	1.844 (42)	1.823 (38)
Pr	0.130 (19)	0.142 (16)	0.131 (15)	0.136 (17)	0.134 (12)	0.125 (14)	0.143 (16)	0.132 (15)	0.145 (15)	0.151 (20)	0.168 (23)	0.179 (19)	0.183 (12)
Nd	0.385 (13)	0.401 (15)	0.382 (15)	0.380 (20)	0.405 (19)	0.398 (16)	0.389 (17)	0.388 (17)	0.433 (44)	0.432 (45)	0.582 (17)	0.618 (34)	0.598 (27)
Sm	0.028 (11)	0.028 (7)	0.029 (12)	0.032 (7)	0.035 (9)	0.034 (9)	0.033 (9)	0.033 (10)	0.033 (12)	0.037 (9)	0.041 (8)	0.045 (7)	0.046 (12)
Gd	0.016 (8)	0.021 (8)	0.012 (8)	0.018 (6)	0.017 (7)	0.015 (9)	0.013 (7)	0.014 (7)	0.018 (7)	0.018 (11)	0.013 (7)	0.015 (9)	0.017 (8)
Th	0.046 (9)	0.045 (6)	0.035 (7)	0.036 (4)	0.050 (6)	0.042 (6)	0.042 (8)	0.041 (3)	0.032 (5)	0.025 (8)	0.073 (14)	0.046 (9)	0.083 (7)
Fe^{3+}	0.440 (50)	0.462 (50)	0.486 (59)	0.470 (51)	0.444 (24)	0.393 (45)	0.404 (40)	0.501 (58)	0.451 (40)	0.481 (84)	0.826 (87)	0.791 (73)	1.007 (45)
A	4.046	4.057	4.048	4.052	4.012	4.011	4.015	4.051	4.033	4.056	4.008	4.031	4.027
(B+C)	4.911	4.908	4.926	4.915	5.000	4.985	4.987	4.911	4.906	4.898	4.954	4.955	4.961

Table 3. Unit cell parameters and results of structure refinement for space group *C*2/*m* in Azores (AZ) and Pakistan (PAK) chevkinites. Number in parentheses refers to standard deviation.

host rock	**AZ LdF5**				**AZ LdF4**		**AZ LdF1**				**PAK**		
sample	**ID**	**45**	**11**	**44**	**4A**	**4GR**	**1**	**75**	**74**	**9**	**6**	**7**	**4**
a(Å)*	13.400 (3)	13.398 (2)	13.404 (3)	13.403 (3)	13.405 (3)	13.402 (2)	13.424 (1)	13.416 (2)	13.416 (3)	13.421 (2)	13.381 (2)	13.387 (2)	13.386 (3)
a(Å)**	13.400 (1)									13.419 (2)			
b(Å)*	5.7258 (9)	5.728 (1)	5.7287 (8)	5.7320 (9)	5.7319 (9)	5.7328 (9)	5.7389 (3)	5.7395 (7)	5.743 (1)	5.7501 (9)	5.7363 (8)	5.7363 (9)	5.7408 (7)
b(Å)**	5.7260 (2)									5.7460 (2)			
c(Å)*	11.059 (2)	11.061 (2)	11.057 (2)	11.057 (2)	11.062 (2)	11.058 (2)	11.067 (1)	11.065 (2)	11.063 (3)	11.065 (1)	11.064 (2)	11.059 (2)	11.068 (2)
c(Å)**	11.0557 (5)									11.0705 (7)			
β(°)*	100.69 (2)	100.64 (1)	100.67 (2)	100.64 (2)	100.67 (1)	100.69 (1)	100.693 (7)	100.66 (1)	100.72 (2)	100.721 (9)	100.61 (1)	100.60 (1)	100.59 (2)
β(°)**	100.641 (5)									100.745 (8)			
V(Å^3)*	833.7 (3)	834.3 (2)	834.4 (2)	834.8 (3)	835.3 (3)	834.9 (2)	837.8 (1)	837.3 (2)	837.5 (4)	839.0 (2)	834.7 (2)	834.7 (2)	836.1 (3)
V(Å^3)**	833.68 (6)									838.65 (8)			
size(mm)	.07,.08,.10	.10,.10,.13	.10,.18,.22	.08,.12,.13	.05,.15,.17	.06,.16,.17	.03,.09,.10	.07,.10,.20	.09,.10,.15	.05,.10,.12	.05,.15,.15	.07,.13..13	.06,.13,.15
ω speed(°/s)	0.029	0.040	0.040	0.033	0.067	0.067	0.025	0.040	0.050	0.040	0.050	0.050	0.050
R_{int}	0.024	0.029	0.027	0.025	0.029	0.026	0.023	0.025	0.030	0.019	0.024	0.021	0.031
N_{all}	1310	1323	1318	1314	1317	1323	1319	1325	1327	1320	1319	1318	1315
$N_{4\sigma}$	1111	1128	1186	1171	1171	1189	1184	1170	1145	1166	1173	1173	1151
R_{all}	0.022	0.023	0.019	0.019	0.022	0.021	0.021	0.022	0.023	0.018	0.022	0.021	0.025
$R_{4\sigma}$	0.015	0.017	0.016	0.015	0.018	0.018	0.016	0.017	0.018	0.014	0.019	0.017	0.021
WR_2	0.037	0.036	0.037	0.034	0.044	0.041	0.034	0.035	0.039	0.027	0.042	0.036	0.046
GooF	0.871	0.885	0.968	0.985	1.002	1.032	0.943	0.976	0.911	0.933	0.961	0.977	0.962
ne$^-$ A1	52.38 (8)	52.38 (8)	52.53 (8)	52.53 (6)	52.15 (8)	51.54 (6)	53.40 (8)	53.17 (8)	54.96 (8)	55.07 (4)	54.24 (8)	54.16 (6)	54.58 (8)
ne$^-$ A2	50.13 (8)	50.29 (8)	50.25 (8)	50.06 (6)	50.13 (8)	49.56 (6)	51.43 (8)	51.31 (8)	53.44 (8)	53.86 (4)	51.54 (8)	51.58 (6)	52.26 (8)
ne$^-$ B	25.95 (13)	26.0 (1)	26.5 (1)	26.1 (1)	26.0 (1)	25.6 (1)	26.3 (1)	26.1 (1)	26.4 (1)	26.0 (8)	24.73 (7)	24.63 (6)	24.61 (7)
ne$^-$ C1	23.41 (1)	23.56 (1)	23.72 (1)	23.73 (1)	23.37 (1)	23.57 (1)	23.61 (1)	23.60 (1)	23.71 (1)	23.718 (8)	23.70 (1)	23.78 (1)	23.75 (1)
ne$^-$ C2A	24.40 (2)	24.76 (2)	25.04 (2)	24.94 (2)	26.37 (6)	26.83 (6)	27.45 (6)	27.26 (6)	27.40 (6)	27.91 (4)	23.24 (1)	23.25 (1)	23.20 (2)
ne$^-$ C2B	23.8 (2)	24.35 (2)	24.48 (2)	24.33 (2)	25.91 (6)	25.84 (6)	26.46 (6)	26.46 (6)	26.16 (6)	27.23 (4)	22.74 (1)	22.74 (1)	22.53 (2)
ne$^-_{ref.}$	326.0 (3)	327.6 (2)	329.1 (2)	328.0 (2)	329.6 (3)	327.6 (2)	337.3 (3)	336.0 (3)	344.2 (2)	346.4 (2)	329.7 (2)	329.7 (2)	331.5 (2)
ne$^-_{chem.}$	326 (4)	331 (4)	328 (4)	326 (4)	332 (3)	330 (4)	336 (3)	337 (4)	341 (6)	345 (9)	333 (5)	336 (5)	336 (4)

* area detector; ** point detector (see text). Agreement factors R, WR2, GooF (Sheldrick 1997). ne$^-_{ref.}$ total electrons per formula unit from structure refinement.

ne$^-_{chem.}$ total electrons per formula unit from average microprobe analysis; for estimated error (in parenthesis) see Appendix A.

Table 4. Calculated cation distribution from minimization procedure in Azores (AZ) and Pakistan (PAK) chevkinites.

host rock	**AZ LdF5**				**AZ LdF4**		**AZ LdF1**				**PAK**		
sample	**ID**	**11**	**45**	**44**	**4A**	**4GR**	**1**	**75**	**74**	**9**	**6**	**7**	**4**
Si1	1.000	1.000	1.000	1.000	1.000	1.000	1.000	1.000	1.000	1.000	1.000	1.000	1.000
A1 site													
Sm	0.014	0.015	0.014	0.016	0.017	0.016	0.016	0.015	0.017	0.018	0.020	0.022	0.022
Th	0.023	0.018	0.022	0.018	0.024	0.020	0.021	0.020	0.016	0.012	0.032	0.022	0.041
Sr	0.000	0.000	0.000	0.000	0.000	0.000	0.000	0.000	0.000	0.000	0.000	0.000	0.000
Ca	0.181	0.173	0.171	0.176	0.182	0.194	0.153	0.153	0.113	0.104	0.133	0.110	0.122
Ce	0.517	0.529	0.515	0.517	0.503	0.509	0.540	0.555	0.554	0.569	0.439	0.451	0.421
La	0.000	0.000	0.000	0.000	0.000	0.000	0.000	0.000	0.000	0.000	0.000	0.000	0.000
Nd	0.192	0.192	0.199	0.193	0.199	0.196	0.193	0.189	0.218	0.213	0.289	0.301	0.295
Pr	0.065	0.066	0.069	0.070	0.066	0.060	0.070	0.063	0.073	0.075	0.080	0.087	0.091
Gd	0.008	0.006	0.010	0.009	0.008	0.006	0.006	0.006	0.009	0.009	0.006	0.007	0.008
B site													
Fe2	0.862	0.764	0.796	0.769	0.858	0.861	0.877	0.884	0.866	0.846	0.822	0.787	0.858
Mg	0.000	0.000	0.000	0.000	0.031	0.038	0.001	0.008	0.000	0.000	0.079	0.078	0.080
Mn	0.059	0.077	0.077	0.070	0.081	0.077	0.091	0.088	0.102	0.110	0.098	0.125	0.062
Ca	0.050	0.075	0.033	0.091	0.000	0.000	0.001	0.000	0.012	0.025	0.000	0.000	0.000
Y	0.024	0.016	0.019	0.025	0.030	0.024	0.030	0.021	0.020	0.019	0.000	0.010	0.000
Zr	0.006	0.068	0.075	0.045	0.000	0.000	0.000	0.000	0.000	0.000	0.000	0.000	0.000
Fe3	0.000	0.000	0.000	0.000	0.000	0.000	0.000	0.000	0.000	0.000	0.000	0.000	0.000
C2A site													
Fe2	0.017	0.101	0.110	0.100	0.120	0.108	0.122	0.140	0.142	0.156	0.152	0.181	0.161
Mg	0.133	0.049	0.069	0.062	0.000	0.000	0.000	0.000	0.000	0.000	0.000	0.000	0.014
Fe3	0.000	0.000	0.000	0.000	0.000	0.000	0.000	0.000	0.000	0.000	0.000	0.000	0.000
Ti	0.650	0.683	0.659	0.668	0.673	0.660	0.615	0.612	0.614	0.568	0.814	0.790	0.786
Nb	0.088	0.128	0.149	0.108	0.117	0.126	0.181	0.178	0.185	0.219	0.014	0.018	0.025
Zr	0.111	0.038	0.012	0.063	0.089	0.106	0.081	0.070	0.059	0.057	0.020	0.010	0.013
Al	0.000	0.000	0.000	0.000	0.000	0.000	0.000	0.000	0.000	0.000	0.000	0.000	0.000

host rock	**AZ LdF5**				**AZ LdF4**		**AZ LdF1**				**PAK**		
sample	**ID**	**11**	**45**	**44**	**4A**	**4GR**	**1**	**75**	**74**	**9**	**6**	**7**	**4**
Si2	1.000	1.000	1.000	1.000	1.000	1.000	1.000	1.000	1.000	1.000	1.000	1.000	1.000
A2 site													
Sm	0.000	0.000	0.000	0.000	0.000	0.000	0.000	0.000	0.000	0.000	0.000	0.000	0.000
Th	0.000	0.000	0.000	0.000	0.000	0.000	0.000	0.000	0.000	0.000	0.000	0.000	0.000
Sr	0.000	0.000	0.000	0.000	0.000	0.000	0.000	0.000	0.000	0.000	0.016	0.016	0.021
Ca	0.194	0.191	0.179	0.198	0.187	0.202	0.159	0.158	0.109	0.095	0.139	0.119	0.106
Ce	0.311	0.312	0.326	0.320	0.316	0.312	0.314	0.318	0.371	0.356	0.440	0.459	0.484
La	0.495	0.497	0.495	0.482	0.497	0.486	0.526	0.524	0.521	0.550	0.404	0.406	0.390
Nd	0.000	0.000	0.000	0.000	0.000	0.000	0.000	0.000	0.000	0.000	0.000	0.000	0.000
Pr	0.000	0.000	0.000	0.000	0.000	0.000	0.000	0.000	0.000	0.000	0.000	0.000	0.000
Gd	0.000	0.000	0.000	0.000	0.000	0.000	0.000	0.000	0.000	0.000	0.000	0.000	0.000
C1 site													
Fe2	0.124	0.176	0.167	0.153	0.191	0.196	0.236	0.201	0.242	0.261	0.019	0.044	0.004
Mg	0.000	0.000	0.000	0.000	0.007	0.000	0.000	0.000	0.000	0.000	0.008	0.006	0.011
Fe3	0.246	0.262	0.265	0.239	0.212	0.210	0.181	0.211	0.191	0.175	0.475	0.443	0.517
Ti	0.576	0.530	0.540	0.562	0.571	0.569	0.576	0.583	0.564	0.561	0.476	0.496	0.443
Nb	0.015	0.009	0.004	0.021	0.000	0.006	0.000	0.000	0.000	0.000	0.000	0.000	0.000
Zr	0.000	0.000	0.000	0.000	0.000	0.000	0.000	0.000	0.000	0.000	0.000	0.000	0.000
Al	0.038	0.022	0.024	0.025	0.019	0.019	0.007	0.005	0.004	0.003	0.022	0.011	0.024
C2B site													
Fe2	0.096	0.077	0.095	0.100	0.061	0.065	0.095	0.074	0.083	0.045	0.046	0.051	0.046
Mg	0.000	0.000	0.000	0.000	0.000	0.000	0.000	0.000	0.000	0.000	0.000	0.000	0.000
Fe3	0.000	0.000	0.000	0.000	0.022	0.000	0.040	0.140	0.139	0.254	0.023	0.022	0.032
Ti	0.829	0.808	0.799	0.797	0.731	0.752	0.652	0.599	0.620	0.494	0.906	0.903	0.909
Nb	0.075	0.115	0.106	0.102	0.186	0.183	0.213	0.187	0.159	0.207	0.025	0.024	0.012
Zr	0.000	0.000	0.000	0.000	0.000	0.000	0.000	0.000	0.000	0.000	0.000	0.000	0.000
Al	0.000	0.000	0.000	0.000	0.000	0.000	0.000	0.000	0.000	0.000	0.000	0.000	0.000

DOI: https://doi.org/10.2138/am-2022-8658. http://www.minsocam.org/

Table 5. Polyhedral bond lengths (Å), volumes (Å^3), angles (°), and octahedral and tetrahedral angular variances in Azores (AZ) and Pakistan (PAK) chevkinites.

host rock	**AZ LdF5**				**AZ LdF4**		**AZ LdF1**				**PAK**		
sample	**ID**	**45**	**11**	**44**	**4A**	**4GR**	**1**	**75**	**74**	**9**	**6**	**7**	**4**
A1-O8	2.482 (3)	2.478 (3)	2.478 (3)	2.478 (3)	2.478 (3)	2.474 (3)	2.483 (3)	2.481 (3)	2.486 (3)	2.484 (3)	2.491 (3)	2.488 (3)	2.489 (4)
A1-O2 x2	2.487 (2)	2.491 (2)	2.492 (2)	2.492 (2)	2.492 (2)	2.491 (2)	2.494 (2)	2.490 (2)	2.489 (2)	2.494 (2)	2.491 (2)	2.493 (2)	2.493 (2)
A1-O3 x2	2.506 (3)	2.501 (3)	2.503 (2)	2.498 (2)	2.502 (3)	2.499 (2)	2.499 (2)	2.500 (3)	2.490 (3)	2.495 (2)	2.505 (3)	2.504 (2)	2.507 (3)
A1-O1 x2	2.573 (2)	2.576 (2)	2.575 (2)	2.577 (2)	2.578 (2)	2.579 (2)	2.581 (2)	2.581 (2)	2.582 (2)	2.585 (2)	2.572 (2)	2.571 (2)	2.576 (3)
A1-O5	2.857 (3)	2.861 (3)	2.857 (3)	2.859 (3)	2.864 (3)	2.857 (3)	2.854 (3)	2.862 (3)	2.856 (3)	2.864 (2)	2.845 (3)	2.849 (3)	2.845 (3)
[A1-O7 x2]	[3.223] (2)	[3.222] (2)	[3.221] (2)	[3.228] (2)	[3.228] (2)	[3.226] (2)	[3.225] (2)	[3.235] (2)	[3.240] (2)	[3.243] (2)	[3.243] (2)	[3.229] (2)	3.241 (2)
[A1-O6]	[3.264] (4)	[3.266] (2)	[3.267] (2)	[3.263] (2)	[3.260] (3)	[3.268] (2)	[3.263] (2)	[3.264] (2)	[3.256] (3)	[3.252] (2)	[3.251] (3)	[3.251] (2)	3.249 (3)
<A1-O>	2.559 (7)	2.560 (7)	2.560 (5)	2.559 (5)	2.561 (7)	2.559 (7)	2.561 (6)	2.561 (7)	2.558 (7)	2.562 (5)	2.559 (7)	2.559 (7)	2.561 (8)
V	25.865 (9)	25.868 (9)	25.864 (7)	25.847 (7)	25.929 (9)	25.853 (8)	25.947 (8)	25.932 (8)	25.871 (9)	25.985 (7)	25.925 (9)	25.909 (8)	25.983 (9)
A2-O8	2.419 (3)	2.410 (3)	2.412 (3)	2.412 (3)	2.420 (3)	2.417 (3)	2.420 (3)	2.414 (3)	2.411 (3)	2.421 (3)	2.412 (3)	2.415 (3)	2.419 (4)
A2-O2 x2	2.521 (2)	2.525 (2)	2.525 (2)	2.523 (2)	2.522 (2)	2.526 (2)	2.525 (2)	2.524 (2)	2.523 (2)	2.529 (2)	2.520 (2)	2.519 (2)	2.518 (2)
A2-O1 x2	2.617 (2)	2.617 (2)	2.616 (2)	2.619 (2)	2.619 (2)	2.617 (2)	2.622 (2)	2.626 (2)	2.625 (2)	2.6334 (2)	2.618 (2)	2.613 (2)	2.614 (3)
A2-O3 x2	2.633 (3)	2.628 (3)	2.625 (2)	2.623 (2)	2.624 (3)	2.624 (2)	2.626 (2)	2.614 (2)	2.619 (3)	2.609 (2)	2.624 (3)	2.631 (2)	2.631 (3)
A2-O4	2.643 (3)	2.644 (3)	2.640 (3)	2.642 (2)	2.639 (3)	2.642 (3)	2.645 (3)	2.652 (3)	2.638 (3)	2.649 (2)	2.644 (3)	2.646 (3)	2.642 (3)
A2-O6 x2	2.980 (1)	2.981 (1)	2.9803 (9)	2.9822 (9)	2.981 (1)	2.982 (1)	2.9832 (9)	2.983 (1)	2.983 (1)	2.9843 (8)	2.984 (1)	2.984 (1)	2.987 (1)
<A2-O>	2.656 (7)	2.655 (7)	2.654 (6)	2.655 (5)	2.655 (7)	2.656 (6)	2.658 (6)	2.656 (7)	2.655 (7)	2.658 (5)	2.655 (7)	2.655 (6)	2.656 (8)
V	35.84 (1)	35.77 (1)	35.73 (1)	35.74 (1)	35.77 (2)	35.79 (1)	35.86 (1)	35.80 (1)	35.73 (2)	35.88 (1)	35.75 (2)	35.74 (1)	35.80 (2)
B-O6 x2	2.016 (3)	2.016 (3)	2.018 (3)	2.015 (3)	2.018 (3)	2.019 (3)	2.019 (3)	2.023 (3)	2.023 (3)	2.026 (3)	2.020 (3)	2.013 (3)	2.019 (4)
B-O3 x4	2.200 (3)	2.202 (3)	2.202 (2)	2.206 (2)	2.210 (2)	2.206 (2)	2.210 (2)	2.213 (2)	2.226 (3)	2.229 (2)	2.211 (3)	2.199 (2)	2.209 (3)
<B-O> weight.	2.139 (87)	2.140 (88)	2.156 (80)	2.152 (86)	2.162 (83)	2.159 (81)	2.162 (86)	2.165 (82)	2.158 (96)	2.180 (87)	2.147 (90)	2.152 (80)	2.157 (85)
<B-O>	2.139 (7)	2.140 (7)	2.141 (6)	2.142 (6)	2.146 (7)	2.144 (6)	2.146 (6)	2.150 (6)	2.158 (7)	2.162 (5)	2.147 (7)	2.137 (7)	2.146 (8)
V	12.43 (1)	12.45 (1)	12.44 (1)	12.46 (1)	12.53 (2)	12.49 (1)	12.54 (1)	12.58 (1)	12.73 (2)	12.76 (1)	12.52 (1)	12.35 (1)	12.49 (2)
$\sigma^2_{\theta\,(oct)}$ (*)	104.6 (6)	107.2 (6)	109.0 (5)	111.1 (4)	109.5 (4)	109.4 (5)	111.3 (5)	113.0 (6)	113.8 (6)	117.5 (4)	115.3 (6)	114.2 (6)	115.5 (7)
C1-O5 x2	1.963 (2)	1.960 (2)	1.963 (2)	1.962 (2)	1.963 (2)	1.962 (2)	1.968 (2)	1.965 (2)	1.969 (2)	1.966 (2)	1.961 (2)	1.959 (2)	1.963 (2)
C1-O4 x2	1.978 (2)	1.978 (2)	1.983 (2)	1.980 (2)	1.985 (2)	1.984 (2)	1.986 (2)	1.982 (2)	1.987 (2)	1.985 (2)	1.979 (2)	1.978 (2)	1.979 (2)
C1-O1 x2	2.017 (2)	2.019 (2)	2.017 (2)	2.017 (2)	2.020 (2)	2.017 (2)	2.023 (2)	2.023 (2)	2.023 (2)	2.025 (2)	2.023 (2)	2.024 (2)	2.022 (2)
<C1-O> weight.	1.986 (23)	1.986 (25)	1.988 (22)	1.986 (23)	1.989 (23)	1.988 (23)	1.992 (23)	1.990 (24)	1.993 (23)	1.993 (25)	1.988 (26)	1.986 (27)	1.988 (25)
<C1-O>	1.986 (5)	1.986 (4)	1.988 (4)	1.987 (4)	1.989 (4)	1.988 (4)	1.992 (4)	1.990 (4)	1.993 (4)	1.992 (4)	1.987 (4)	1.987 (4)	1.988 (4)
V	10.38 (1)	10.378 (9)	10.408 (8)	10.390 (7)	10.441 (9)	10.413 (8)	10.481 (8)	10.448 (9)	10.490 (9)	10.476 (8)	10.405 (9)	10.392 (8)	10.412 (9)
$\sigma^2_{\theta\,(oct)}$ (*)	14.0 (2)	14.3 (2)	13.9 (2)	14.3 (2)	13.7 (2)	13.8 (2)	14.4 (2)	14.0 (2)	15.2 (2)	14.8 (2)	14.1 (2)	14.5 (2)	14.4 (2)
O4-O5 sh.	2.685	2.680	2.690	2.684	2.693	2.690	2.696	2.687	2.696	2.686	2.678	2.675	2.680
O4-O5 unsh.	2.884	2.886	2.886	2.888	2.888	2.888	2.892	2.891	2.895	2.898	2.889	2.889	2.891
C2A-O2 x4	2.007 (2)	2.004 (2)	2.003 (2)	2.007 (2)	2.008 (2)	2.007 (2)	2.010 (2)	2.011 (2)	2.012 (2)	2.014 (2)	2.000 (2)	2.004 (2)	2.004 (2)
C2A-O5 x2	2.014 (3)	2.019 (3)	2.017 (3)	2.018 (2)	2.016 (3)	2.018 (3)	2.018 (3)	2.020 (3)	2.015 (3)	2.022 (3)	2.016 (3)	2.020 (3)	2.015 (3)
<C2A-O>weight.	2.009 (3)	2.008 (7)	2.006 (6)	2.010 (5)	2.010 (3)	2.010 (5)	2.012 (4)	2.013 (4)	2.013 (1)	2.016 (3)	2.004 (7)	2.008 (7)	2.007 (5)
<C2A-O>	2.009 (6)	2.009 (5)	2.008 (4)	2.010 (4)	2.011 (5)	2.011 (5)	2.012 (5)	2.014 (5)	2.013 (6)	2.017 (4)	2.005 (5)	2.009 (5)	2.008 (5)
V	10.76 (1)	10.76 (1)	10.740 (8)	10.778 (8)	10.80 (1)	10.78 (1)	10.818 (9)	10.84 (1)	10.82 (1)	10.883 (8)	10.69 (1)	10.76 (1)	10.72 (1)
$\sigma^2_{\theta\,(oct)}$ (*)	10.5 (2)	11.1 (2)	10.9 (1)	11.1 (2)	10.2 (2)	11.5 (2)	10.9 (2)	10.7 (2)	10.9 (2)	12.1 (2)	11.8 (2)	11.6 (2)	12.2 (2)
O2-O2 sh.	2.771	2.765	2.762	2.766	2.771	2.767	2.774	2.781	2.779	2.775	2.745	2.751	2.747
O2-O2 unsh.	2.903	2.903	2.902	2.907	2.908	2.908	2.909	2.905	2.909	2.921	2.908	2.915	2.916

C2B-O2 x4	1.978 (2)	1.976 (2)	1.976 (2)	1.976 (2)	1.978 (2)	1.977 (2)	1.982 (2)	1.985 (2)	1.985 (2)	1.982 (2)	1.971 (2)	1.970 (2)	1.970 (2)
C2B-O4 x2	2.021 (3)	2.021 (3)	2.016 (3)	2.020 (2)	2.015 (3)	2.014 (3)	2.019 (2)	2.022 (3)	2.020 (3)	2.024 (3)	2.016 (3)	2.018 (3)	2.019 (3)
<C2B-O>weight.	1.989 (19)	1.987 (19)	1.985 (17)	1.988 (20)	1.987 (16)	1.986 (16)	1.994 (17)	1.994 (16)	1.994 (15)	1.991 (18)	1.982 (20)	1.982 (20)	1.982 (21)
<C2B-O>	1.992 (6)	1.991 (5)	1.989 (5)	1.991 (4)	1.990 (5)	1.989 (5)	1.994 (5)	1.997 (5)	1.997 (6)	1.996 (4)	1.986 (5)	1.986 (5)	1.986 (5)
V	10.49 (1)	10.48 (1)	10.447 (8)	10.480 (8)	10.46 (1)	10.452 (9)	10.523 (9)	10.58 (1)	10.55 (1)	10.552 (8)	10.40 (1)	10.403 (9)	10.40 (1)
$\sigma^2_{\theta\,(oct)}$ (*)	9.9 (2)	9.8 (1)	10.4 (1)	10.0 (1)	10.9 (2)	9.9 (1)	11.0 (1)	9.7 (1)	11.6 (2)	9.9 (1)	10.2 (2)	9.8 (1)	10.1 (2)
O2-O2 unsh.	2.823	2.825	2.827	2.825	2.824	2.825	2.830	2.834	2.834	2.829	2.828	2.821	2.825
Si1-O6	1.578 (4)	1.577 (3)	1.577 (3)	1.580 (3)	1.579 (4)	1.576 (3)	1.582 (3)	1.571 (3)	1.575 (4)	1.575 (3)	1.575 (3)	1.583 (3)	1.581 (4)
Si1-O7	1.602 (4)	1.598 (4)	1.600 (3)	1.599 (3)	1.603 (4)	1.603 (4)	1.599 (3)	1.606 (3)	1.599 (4)	1.599 (3)	1.601 (4)	1.595 (3)	1.600 (4)
Si1-O1 x2	1.631 (2)	1.630 (2)	1.6311 (19)	1.631 (2)	1.630 (2)	1.630 (2)	1.630 (2)	1.629 (2)	1.633 (3)	1.630 (2)	1.630 (2)	1.632 (2)	1.633 (3)
<Si1-O>weight.	1.617 (20)	1.614 (22)	1.615 (22)	1.615 (21)	1.617 (20)	1.614 (22)	1.614 (20)	1.613 (23)	1.613 (24)	1.614 (22)	1.614 (22)	1.615 (21)	1.615 (22)
<Si1-O>	1.611 (6)	1.609 (5)	1.610 (5)	1.610 (5)	1.610 (6)	1.610 (5)	1.610 (5)	1.609 (5)	1.610 (6)	1.609 (5)	1.609 (6)	1.610 (5)	1.612 (15)
V	2.142 (6)	2.133 (6)	2.139 (5)	2.139 (5)	2.142 (6)	2.139 (5)	2.140 (5)	2.135 (6)	2.139 (6)	2.134 (5)	2.137 (6)	2.141 (5)	2.146 (6)
$\sigma^2_{\theta\,(tet)}$ (**)	2.3 (2)	2.0 (2)	2.2 (2)	1.9 (2)	2.1 (2)	1.7 (2)	2.6 (2)	2.1 (2)	2.0 (2)	2.1 (2)	1.6 (2)	2.8 (2)	1.6 (2)
O6-Si1-O7	110.3 (2)	110.500 (2)	110.67 (17)	110.25 (17)	110.5 (2)	110.38 (19)	111.06 (17)	110.30 (19)	110.6 (2)	110.57 (16)	110.2 (2)	111.0 (2)	110.6 (2)
O6-Si1-O1 x2	110.04 (11)	109.91 (11)	109.88 (9)	109.97 (9)	109.85 (11)	109.79 (10)	109.72 (9)	110.03 (10)	109.71 (11)	109.86 (9)	109.93 (11)	109.79 (10)	109.62 (13)
O1-Si1-O1	111.22 (17)	111.04 (16)	111.11 (14)	111.08 (14)	111.16 (16)	111.10 (15)	111.22 (14)	111.08 (15)	111.19 (18)	111.12 (13)	110.93 (15)	111.31 (15)	110.95 (18)
O7-Si1-O1 x2	107.59 (12)	107.72 (12)	107.64 (10)	107.76 (10)	107.73 (12)	107.88 (11)	107.54 (10)	107.66 (11)	107.82 (12)	107.69 (10)	107.91 (12)	107.46 (11)	108.01 (13)
Si2-O8	1.583 (3)	1.593 (3)	1.590 (3)	1.593 (3)	1.589 (3)	1.590 (3)	1.588 (3)	1.590 (3)	1.594 (3)	1.587 (3)	1.593 (3)	1.588 (3)	1.592 (4)
Si2-O7	1.611 (4)	1.609 (4)	1.611 (3)	1.612 (3)	1.607 (4)	1.607 (4)	1.615 (3)	1.610 (4)	1.611 (4)	1.615 (3)	1.610 (4)	1.612 (3)	1.609 (4)
Si2-O3 x2	1.618 (3)	1.623 (3)	1.623 (2)	1.626 (2)	1.619 (3)	1.625 (2)	1.624 (2)	1.626 (2)	1.619 (3)	1.620 (2)	1.624 (2)	1.632 (2)	1.627 (3)
<Si2-O>weight.	1.607 (15)	1.612 (13)	1.614 (13)	1.615 (14)	1.609 (13)	1.615 (14)	1.615 (14)	1.616 (15)	1.611 (10)	1.612 (13)	1.615 (13)	1.619 (17)	1.616 (14)
<Si2-O>	1.608 (6)	1.612 (6)	1.612 (5)	1.614 (5)	1.608 (6)	1.612 (6)	1.613 (5)	1.613 (6)	1.611 (6)	1.611 (5)	1.613 (6)	1.616 (6)	1.614 (7)
V	2.118 (6)	2.132 (6)	2.133 (5)	2.143 (5)	2.119 (6)	2.131 (5)	2.135 (5)	2.139 (6)	2.129 (6)	2.129 (5)	2.135 (6)	2.147 (5)	2.139 (6)
$\sigma^2_{\theta\,(tet)}$ (**)	21.1 (6)	22.6 (6)	23.0 (5)	23.0 (5)	21.9 (6)	22.7 (6)	23.6 (5)	22.2 (5)	22.0 (6)	21.7 (4)	21.8 (6)	24.3 (6)	23.0 (7)
O8-Si2-O7	112.9 (2)	113.01 (19)	112.92 (16)	112.72 (16)	112.6 (2)	112.59 (19)	112.83 (17)	112.52 (18)	112.6 (2)	112.26 (16)	112.6 (2)	113.28 (18)	112.7 (2)
O8-Si2-O3 x2	113.69 (11)	113.81 (11)	113.92 (9)	114.03 (9)	113.95 (11)	114.03 (10)	113.99 (10)	114.07 (10)	113.92 (12)	114.10 (9)	113.98 (11)	113.88 (10)	113.98 (13)
O7-Si2-O3 x2	104.33 (13)	104.19 (13)	104.19 (11)	104.25 (11)	104.37 (14)	104.23 (12)	104.00 (11)	104.55 (12)	104.27 (14)	104.55 (10)	104.40 (13)	103.93 (12)	104.15 (15)
O3-Si2-O3	107.1 (2)	106.9 (2)	106.75 (18)	106.60 (17)	106.7 (2)	106.80 (19)	107.06 (18)	106.14 (19)	106.9 (2)	106.38 (16)	106.6 (2)	106.96 (19)	106.9 (2)
Si2-A2	3.233 (2)	3.231 (1)	3.230 (1)	3.2 (1)	3.231 (1)	3.230 (1)	3.228 (1)	3.230 (1)	3.224 (2)	3.221 (1)	3.234 (1)	3.235 (1)	3.237 (2)
O3-O3 sh.	2.603	2.606	2.605	2.608	2.598	2.609	2.611	2.600	2.602	2.594	2.604	2.623	2.614
Si1-O7-Si2	169.1 (3)	169.2 (3)	169.3 (2)	168.7 (2)	168.7 (3)	168.8 (3)	169.4 (2)	168.1 (3)	167.8 (3)	167.5 (2)	167.7 (3)	169.7 (3)	168.4 (3)

(*) octahedral and (**) tetrahedral angular variance where θ_i is each individual bond angle (Robinson et al. 1971): (*) $\sigma^2_{\theta(oct)} = \sum_{i=1}^{12} (\theta_i - 90°)^2 / 11$ (**) $\sigma^2_{\theta(tet)} = \sum_{i=1}^{6} (\theta_i - 109.47°)^2 / 5$

Table 6. Hyperfine parameters of Pakistan chevkinite at 11K; δ is quoted to α-Fe, calculated χ^2=1.04.

	δ (mm/s)	**Δ (mm/s)**	**Γ (mm/s)**	**A (%)**	**Oxidation ratio**	**Fe(II)/Fe(III)**	**Attribution**
Db1	0.43±0.04	0.86±0.08	0.61±0.05	55±4			Fe(III) oct.
Db2	1.09±0.01	2.82±0.09	0.27±0.09	10±1	0.55	0.82	Fe(II) oct.
Db3	1.26±0.01	2.11±0.03	0.35±0.04	35±3			Fe(II) oct.

Table 7. Bond valences (vu) and bond valence sums (BVS) for representative Azores (44, 9) and Pakistan (4) samples.

		A1	A2	B	C1	C2A	C2B	Si1	Si2	BVS	BVS'
O1	44	0.29 $^{x2}\downarrow$	0.27 $^{x2}\downarrow$		0.54 $^{x2}\downarrow$			0.98 $^{x2}\downarrow$		2.08	
	9	0.29	0.27		0.52			0.98		2.07	
	4	0.29	0.28		0.52			0.98		2.07	
O2	44	0.36 $^{x2}\downarrow$	0.35 $^{x2}\downarrow$			0.61 $^{x4}\downarrow$	0.65 $^{x4}\downarrow$			1.97	
	9	0.37	0.36			0.62	0.65			1.99	
	4	0.36	0.36			0.59	0.65			1.97	
O3	44	0.36 $^{x2}\downarrow$	0.27 $^{x2}\downarrow$	0.32 $^{x4}\downarrow$					1.00 $^{x2}\downarrow$	1.94	
	9	0.37	0.29	0.28					1.01	1.95	
	4	0.35	0.27	0.28					0.99	1.89	
O4	44		0.25		0.60 $^{x2}\downarrow\rightarrow$		0.58 $^{x2}\downarrow$			2.03	
	9		0.26		0.58		0.58			2.00	
	4		0.26		0.59		0.57			2.00	
O5	44	0.13			0.63 $^{x2}\downarrow\rightarrow$	0.59 $^{x2}\downarrow$				1.98	
	9	0.14			0.61	0.60				1.97	
	4	0.14			0.61	0.57				1.94	
O6	44	[0.05]	0.10 $^{x2}\rightarrow$	0.54 $^{x2}\downarrow$				1.13		1.87	1.91
	9	[0.05]	0.10	0.48				1.14		1.83	1.88
	4	[0.05]	0.10	0.46				1.12		1.79	1.84
O7	44	[0.05] $^{x2}\downarrow$						1.07	1.03	2.10	2.15
	9	[0.05]						1.07	1.02	2.09	2.14
	4	[0.05]						1.07	1.04	2.11	2.16
O8	44	0.37	0.47						1.09	1.93	
	9	0.38	0.48						1.11	1.96	
	4	0.37	0.47						1.09	1.93	
BVS	44	2.52	2.69	2.37	3.53	3.60	3.78	4.16	4.11		
BVS'		2.66									
V		2.84	2.80	2.11	3.45	3.78	3.90	4.00	4.00		
BVS	9	2.57	2.78	2.08	3.44	3.67	3.75	4.18	4.15		
BVS'		2.71									
V		2.91	2.91	2.02	3.30	3.91	3.86	4.00	4.00		
BVS	4	2.52	2.76	2.04	3.45	3.48	3.75	4.14	4.12		
BVS'		2.67									
V		2.92	2.87	2.00	3.43	3.67	3.89	4.00	4.00		

BVS and BVS' calculated from the bond valence parameters of Brese and O'Keeffe (1991), respectively, without and with bond valences for A1-O6 and A1-O7 bond lengths around 3.2 Å (in square brackets) (see text and Table 5). V: formal charge.

Table 8. Comparison of Fe percent distribution, relative to Fe_{tot}, between Mössbauer spectroscopy at 11K (observed) and cation distribution (calculated) in the Pakistan chevkinite.

	Fe^{2+}(B)	Fe^{2+}(C1)	Fe^{2+}(C2A)	Fe^{2+}(C2B)	Fe^{3+}(B)	Fe^{3+}(C1)	Fe^{3+}(C2A)	Fe^{3+}(C2B)
Mössbauer spectroscopy	35 ±3		10 ±1			55 ±4		
sample 6	41	2	8	2	0	47	0	1
sample 7	39	4	9	3	0	44	0	1
sample 4	40	0	8	2	0	48	0	2